




1 **Assessing Locations Susceptible to Landslide Initiation During**
2 **Prolonged Intense Rainfall in the Lares, Utuado, and Naranjito**
3 **Municipios of Puerto Rico** 
4

5 Rex L. Baum¹, Dianne L. Brien², Mark E. Reid², William H. Schulz¹, and Matthew J. Tello^{1,3}

6 ¹U.S. Geological Survey, Golden, Colorado 80401, USA²U.S. Geological Survey, Moffett Field, California 94035,
7 USA

8 ³Present Address, Colorado Department of Transportation, Denver, Colorado 80204, USA

9 *Correspondence to:* Rex L. Baum (baum@usgs.gov)

10



11 **Abstract.** Hurricane María induced about 70,000 landslides throughout Puerto Rico, USA, including thousands each
12 in three municipalities situated in Puerto Rico’s rugged Cordillera Central range. By combining a nonlinear soil-depth
13 model, presumed wettest-case pore pressures, and quasi-three-dimensional (3D) slope-stability analysis we developed
14 a landslide susceptibility map that has very good performance and continuous susceptibility zones having smooth,
15 buffered boundaries. Our landslide susceptibility map enables assessment of (1) potential ground-failure locations,
16 and (2) areas of potential landslide sources to support a companion assessment of inundation and debris-flow runoff.
17 The quasi-3D factor of safety, F_3 , showed strong inverse correlation to landslide density (high density at low F_3). Area
18 under the curve (AUC) of True Positive Rate (TPR) versus False Positive Rate indicated success of F_3 in identifying
19 head-scarp points (AUC=0.84) and source-area polygons ($0.85 \leq \text{AUC} \leq 0.88$). The susceptibility zones enclose
20 specific percentages of observed landslides. Thus, zone boundaries use successive F_3 levels for increasing TPR of
21 landslide head-scarp points, with zones bounded by F_3 at TPR=0.75, very high; F_3 at TPR=0.90, high; and the
22 remainder moderate to low. The very high susceptibility zone, with 118 landslides/km², covered 23% of the three
23 municipalities. The high zone (51 landslides/km²) covered another 10%.

24 1 Introduction

25 Heavy rainfall from Hurricane María during September 2017 produced tens of thousands of landslides on the main
26 island of Puerto Rico, USA (Bessette-Kirton et al. 2017, 2019a; Hughes et al. 2019). Shallow, translational failures in
27 soil or saprolite, from decimeters to a few meters deep were the most common landslides. Deeper (up to 30 m) complex
28 failures in soil, saprolite, and rock, as well as rock falls and rock slides also occurred (Bessette-Kirton et al. 2017).
29 Many landslides transformed into debris flows that commonly coalesced and flowed down channels. Landslides
30 caused fatalities as well as widespread damage to homes, roads, and other infrastructure.

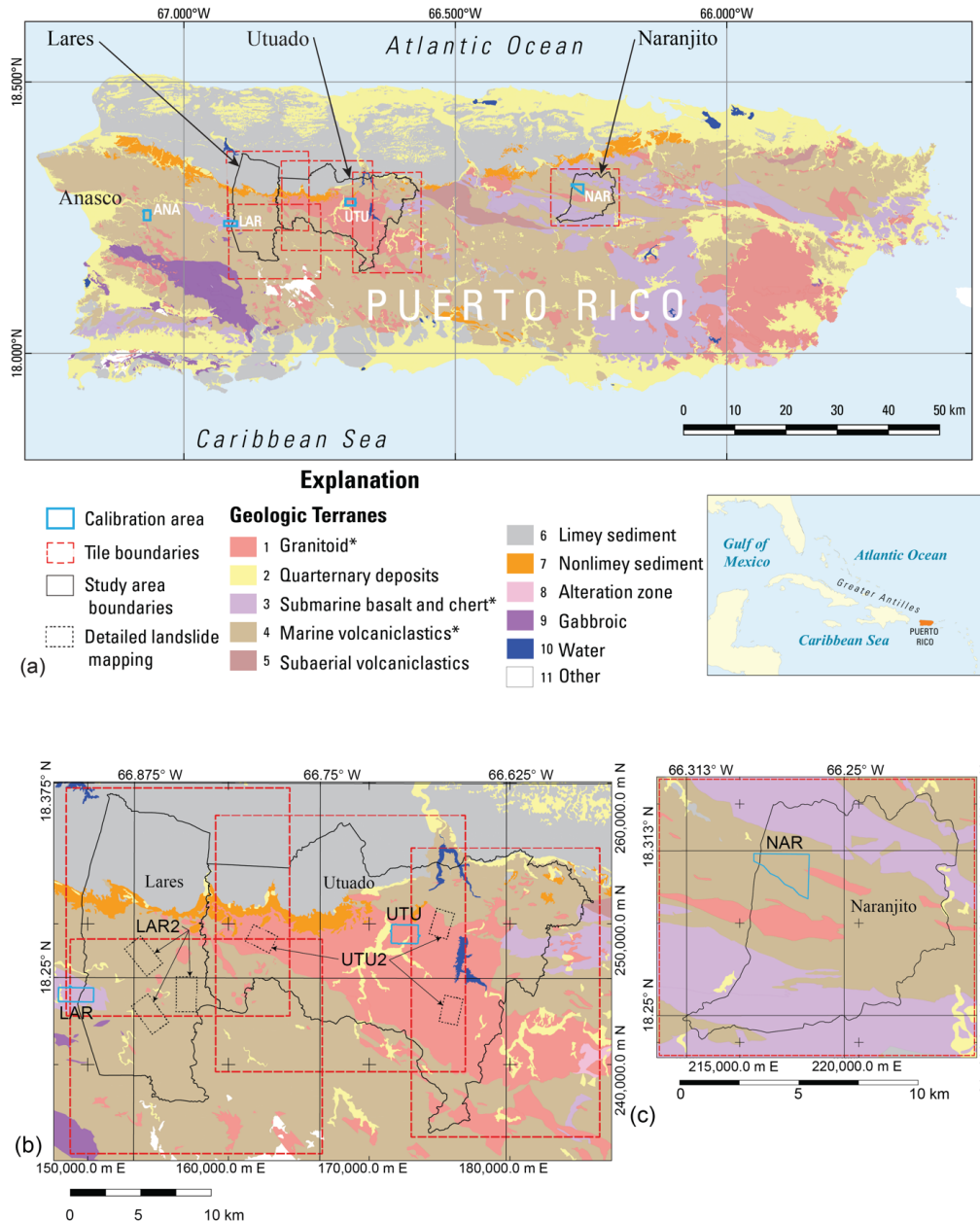
31 In the aftermath of the hurricane, the U.S. Geological Survey (USGS) began working with local partners to conduct
32 detailed assessments of landslide and debris-flow hazards, both island-wide (Hughes and Schulz 2020a, b) and more
33 locally (this study) for three impacted municipalities (Lares Municipio, Utuado Municipio, and Naranjito Municipio)
34 in the central mountains of Puerto Rico. Here we describe the landslide initiation (source area) part of a landslide
35 susceptibility assessment for these municipalities. Estimating landslide initiation potential is part of a larger effort (in
36 progress, Brien et al. 2021) to estimate overall hazard from (1) landslide initiation (ground failure), (2) landslide
37 runoff, and (3) debris-flow inundation from future extreme rainfall, including tropical cyclones (hurricanes), as well
38 as localized storms expected to impact these areas of Puerto Rico.

39 **One of the objectives of this work is to produce integrated maps of potential landslide initiation and inundation areas.**
40 **Although much progress has been made in methods for assessing landslide susceptibility (e.g., Carrara et al. 1999;**
41 **Chung and Fabri 2003; Lee et al. 2003; Godt et al. 2008; Baum et al. 2014; Canli et al. 2018) as well as debris-flow**
42 **inundation (George and Iverson 2014; Reid et al. 2016; Aaron et al. 2017; Bessette-Kirton et al. 2019b), combining**
43 **these two types of assessments into a single map for an area of hundreds of square kilometers remains challenging**
44 **(Ellen et al. 1993; Benda et al. 2007; Fan et al. 2017; Hsu and Liu 2019; Mergili et al. 2019).** One of the challenges is
45 estimating potential source-area extent and depth. We addressed this challenge by modelling soil depth and using it to
46 approximate potential source-area depth in one-dimensional (1D) and quasi-three-dimensional (3D) slope stability



47 models for use in assessing regional shallow landslide susceptibility. Such an approach helps ensure that the
48 susceptibility model accounts for variable failure depth across the landscape and that predicted areas of potential
49 landslide sources are acceptable for use in assessing debris-flow inundation. The quasi-3D model uses a simplified
50 limit-equilibrium analysis to estimate the stability of a slab-shaped trial landslide. Another challenge is establishing
51 meaningful susceptibility categories, which we addressed by delimiting the categories at quasi-3D factor of safety
52 values, F_3 , that enclose specific percentages of landslide sources, rather than relying on theoretical or arbitrary factor
53 of safety values to delimit the categories. By showing like outcomes (areas that capture specific percentages of
54 observed landslides), maps based on this approach are directly comparable to each other.

55 This study was conducted in stages between 2018 and 2022 and involved three study areas as well as calibration areas,
56 study-area tiles, and validation areas. We define these here to help the reader comprehend how our presentation of the
57 study is organized. The study areas comprise three municipalities, Lares Municipio, Utuado Municipio, and Naranjito
58 Municipio, and are the focus of our landslide initiation susceptibility maps (Supplemental Figures S1 and S2; Baum
59 et al. 2023). These municipalities were chosen because they were severely impacted by Hurricane María landslides
60 and to help manage their future growth and development. We enclosed the Lares and Utuado study areas in four
61 overlapping rectangles and enclosed Naranjito Municipio in a fifth, separate rectangle (Fig. 1a, 1b, and 1c). The
62 rectangles extend beyond the drainage divides of basins that straddle municipality boundaries. The rectangles delimit
63 overlapping tiles of the digital elevation models (DEM) used in the susceptibility analysis. These DEM tiles helped
64 keep file sizes (6 gigabytes or less for ASCII input and output grids) manageable and overlap ensured that edge effects
65 would not degrade soil-depth or slope-stability computations. The extended boundaries ensured that landslide runout
66 and debris-flow inundation models (Brien et al. 2021) would not be impeded by municipality boundaries or other
67 artificial barriers. The calibration areas (Fig. 1) were placed in distinct geologic terranes where high concentrations of
68 landslides had occurred. Previous detailed mapping and characterization (Bessette-Kirton et al. 2019c, 2020) and field
69 studies (Baum et al. 2018) in these areas provided data for testing and calibrating soil-depth and slope-stability models
70 (Tello 2020). From east to west, each 2-km² calibration area was named for a nearby city: Añasco (ANA), Lares
71 (LAR), Utuado (UTU), and Naranjito (NAR). Although ANA is about 15 km west of the study areas, it was included
72 to provide additional calibration data in an area of high landslide density for submarine volcanoclastic lithologies
73 because sufficient data were not available at NAR. Soils, land cover, and other characteristics (besides bedrock
74 lithology) that influence landslide susceptibility vary between the four calibration areas (Bessette-Kirton et al. 2020;
75 Hughes and Schulz 2020a, 2020b). We used six additional areas of detailed mapping (Einbund et al. 2021a, 2021b) to
76 help evaluate the final maps. These validation areas are designated LAR2 and UTU2, and each includes three
77 rectangular areas of detailed landslide mapping. (Fig. 1b). We combined detailed source area mapping of NAR
78 (Baxstrom et al. 2021a) and UTU (Einbund et al. 2021a) with that in LAR2 and UTU2 for the validation.
79



80

81 **Figure 1. Geologic map showing municipality boundaries, study areas, calibration areas, and major lithologies (geologic**
 82 **terranes) for the main island of Puerto Rico. Simplified from Bawiec (1998) by combining submarine volcanoclastic rocks**
 83 **of various ages into a single map unit. Primary landslide-prone lithologies indicated by * in map explanation. Municipality**
 84 **boundaries of Lares, Utuado, and Naranjito define study areas. Digital elevation models covering the study areas were**
 85 **divided into five smaller tiles. Extent of Anasco (ANA), Lares (LAR), Utuado (UTU), and Naranjito (NAR) calibration areas**
 86 **from Besette-Kirton et al. (2019c, 2020). (a) overview of entire island, (b) details of Lares and Utuado study areas including**
 87 **outlines of areas of detailed landslide mapping in Utuado, (UTU2, Einbund et al. 2021a) and Lares (LAR2, Einbund et al.**
 88 **2021b), (c) details of Naranjito study area.**



89 In the following sections, we describe characteristics of the study areas, summarize our methods and results, and
90 discuss advantages, limitations, and implications of our approach. First, we describe the setting, geology, and
91 landslides of Puerto Rico including details specific to the study areas. Then we describe the available topographic and
92 geotechnical data followed by a description of the workflow for assessing landslide susceptibility. Next, we describe
93 our methods for modelling soil depth, pressure head, and slope stability along with procedures for model calibration
94 and details of how the calibrated models were applied to and evaluated for our study areas. Then we present results of
95 the calibration, soil-depth modelling, 1D and quasi-3D stability analyses, and the evaluation and validation of the
96 susceptibility analysis. These results were obtained using pre-event light detection and ranging (lidar) DEMs (U.S.
97 Geological Survey, 2018); we reran our models using calibrated input parameters and post-event lidar (U.S.
98 Geological Survey 2020a, b, c) to estimate susceptibility to future landslides. We finish by discussing strengths and
99 limitations of our approach as well as some unexpected findings and ways to simplify the workflow for application to
100 areas where limited data are available.

101 **2 Study area**

102 Puerto Rico is a U.S. territory and lies at the east end of the Greater Antilles island chain in the Caribbean Sea (Fig.
103 1). The main island is characterized by rugged topography and covers an area of 8750 km². The study areas and
104 calibration areas lie in the east–west-trending Cordillera Central range, which spans most of the island. The range
105 exceeds elevations of 900 m at many places, and its highest peak reaches an elevation of 1340 m. Coastal plains and
106 broad lowlands ring most of the island. Ongoing tectonic uplift is one of the main factors creating the rugged
107 topography across the island (Taggart and Joyce 1991). Warm temperatures, high rainfall, and humidity contribute to
108 deep weathering and widespread saprolite formation (Murphy et al. 2012).

109 **2.1 Geology and soils**

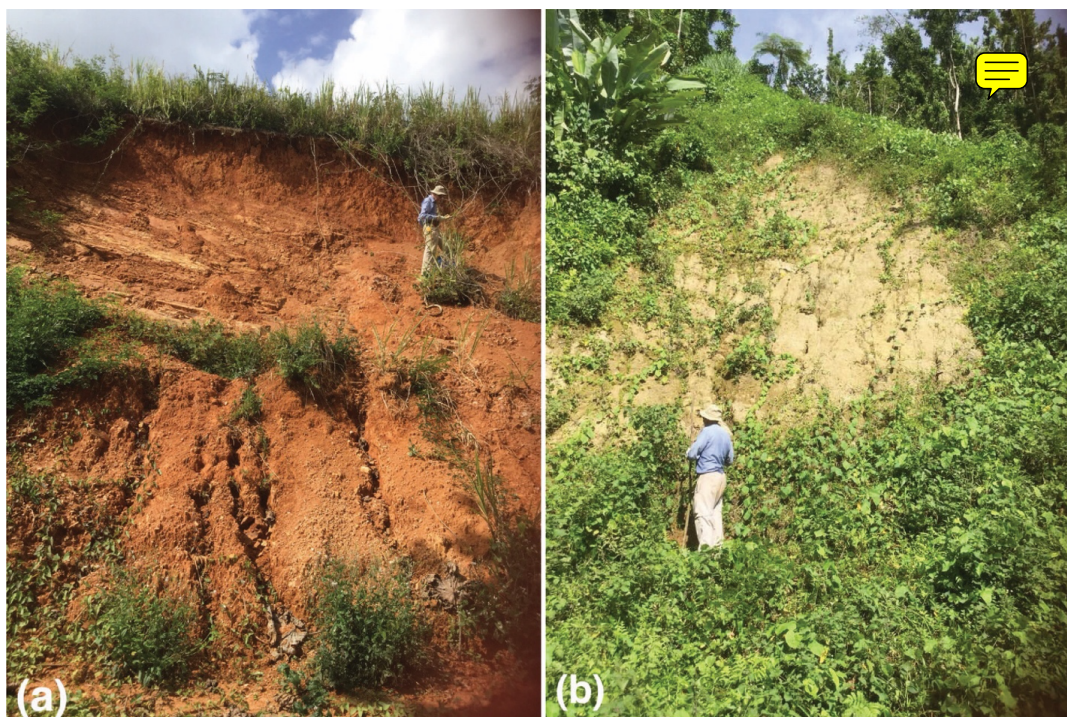
110 Heavily faulted basement rocks, consisting mainly of oceanic crust, volcanoclastic, and intrusive rocks, underlie the
111 Cordillera Central range (Jolly et al. 1998). A cover sequence of carbonates and associated clastic sediments
112 unconformably overlies the basement complex. The carbonates have weathered to form tropical karst in the lowlands
113 north of the range (Monroe 1976). Bawiec (1998) generalized the geology of Puerto Rico into twelve geologic terranes
114 having related rock types. We have simplified the terranes slightly for purposes of this study (Fig. 1). Soil mapping
115 and databases published by the U.S. Department of Agriculture’s Natural Resources Conservation Service (NRCS)
116 indicate a wide range in the textures (particle-size distributions) and hydraulic properties of soils in the study areas
117 (Soil Survey Staff 2018). Most hillside soils have developed by in-place chemical weathering of underlying bedrock
118 or saprolite and locally derived colluvium. Despite the steep slopes, in many places the upper few meters of bedrock
119 have weathered to saprolite (e.g., Jibson 1989; Larsen and Torres-Sanchez 1992).

120 **2.2 Landslides**

121 Recent and historical studies described and characterized Puerto Rico’s rainfall-induced landslides. Published studies
122 of past landslides characterized rainfall-induced landslides in southern and eastern parts of Puerto Rico (Jibson 1989;



123 Simon et al. 1990; Larsen and Torres-Sanchez 1992, 1998; Pando et al. 2005; Larsen 2012). Several post-Hurricane
124 María studies documented dimensional, geologic, and topographic characteristics of landslide sources in ten
125 representative areas of high landslide density within and near the municipality study areas (Fig. 1): Baum et al. (2018)
126 conducted field studies and measurements (Fig. 2), and Bessette-Kirton et al. (2019c) later mapped landslides using
127 post-event aerial photography in the four areas denoted as ANA, LAR, NAR, and UTU (Fig. 1a). U.S. Geological
128 Survey staff later remapped NAR (Baxstrom et al. 2021a), remapped UTU (Einbund et al. 2021a), and mapped six
129 additional areas (UTU2 and LAR2, Fig. 1b) near UTU and LAR (Einbund et al. 2021a, 2021b). Schulz et al. (2023)
130 expanded on earlier field studies of Baum et al. (2018). Data from some of these studies supported recent analyses of
131 landslide susceptibility (Bessette-Kirton et al. 2019a; Hughes and Schulz 2020a) and runout characteristics (Bessette-
132 Kirton et al. 2020).
133

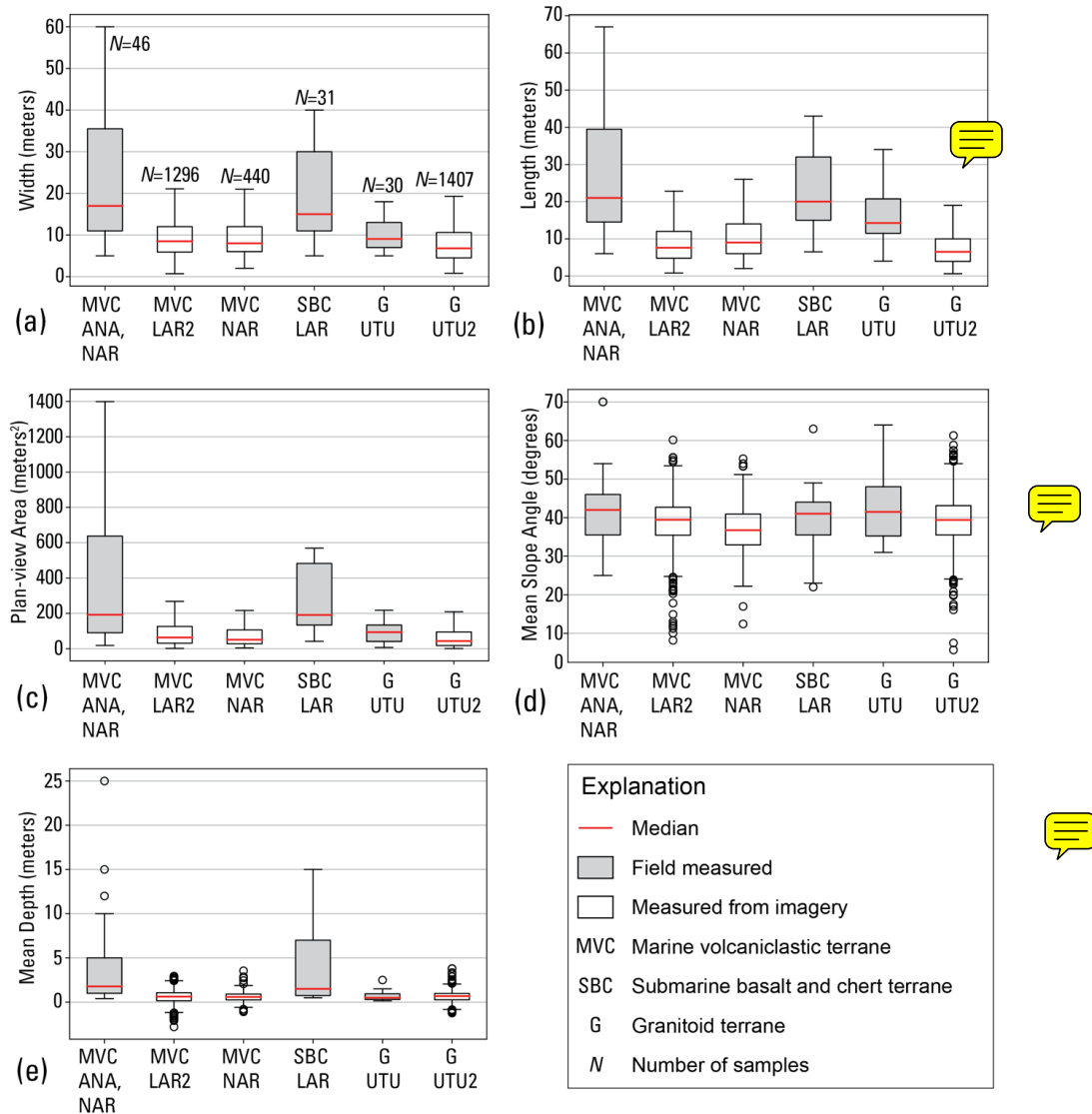


134
135 **Figure 2. Photographs taken in May 2018 depicting source areas of shallow landslides in (a) volcaniclastic terrane and (b)**
136 **granitoid terrane eight months after Hurricane María (photographs by C. Cerovski-Darriau, U.S. Geological Survey, public**
137 **domain).**

138 The post-Hurricane María studies cited above indicated that most source areas were fully evacuated, and shallow
139 translational slides appear to be the most common type of movement prior to transforming to debris flows.
140 Nevertheless, source area shapes were consistent with translational, rotational, or complex movement. Source areas
141 exposed soil, saprolite, and bedrock (Fig. 2). Soil matrix textures ranged from sand to clay; clast content increased
142 with depth. Differences between the landslide source sizes and depths within the different terranes (Fig. 3) seem



143 consistent with their different lithologies and depth of weathering (volcaniclastic rocks, weathered volcanic rocks,
 144 granitic pluton).
 145



146
 147 **Figure 3.** Box plots summarizing landslide source dimensions obtained for three geologic terranes by field studies of 107
 148 landslides (gray, Baum et al. 2018) and by mapping 3440 landslides from aerial imagery and lidar-derived digital elevation
 149 models (white, Baxstrom 2021a; Einbund 2021a, 2021b). (a) width, (b) length, (c) plan-view area calculated directly by
 150 geographic information system for mapped polygons and estimated from field measurements as an ellipse and projected to
 151 the horizontal, $\pi \times (\text{Length} \times \text{Width} \times \cos(\text{Slope angle}))/4$, (d) mean slope angle, (e) mean landslide source depths. Outliers
 152 of width, length and area not shown to keep 25%, 50%, and 75% quartiles legible. [Locations (as shown in Fig. 1): ANA,
 153 Añasco; LAR, Lares; LAR2, Lares (Einbund et al. 2021b); UTU, Utuado; UTU2, Utuado (Einbund et al. 2021b, includes
 154 UTU); NAR, Naranjito (remapped by Baxstrom et al. 2021a)].



155 Figure 3 summarizes landslide dimensions obtained from the post-Hurricane María studies for the three main geologic
156 terranes in the study areas (Fig. 1). The field measurements (using laser range finder, tape, and clinometer; Baum et
157 al. 2018), though biased by purposely including several large landslides (1500 m² – 6600 m²), represent the range of
158 sizes of Hurricane María landslide sources. Mapping from imagery (Baxstrom et al. 2021a; Einbund et al. 2021a,
159 2021b) included all landslides visible in the imagery of several 2.5-km² target areas and represent typical dimensions
160 of landslides triggered by the hurricane on uplands and valley side slopes. Most landslide sources had lengths and
161 widths less than 10-15 m, with median mapped length and width among the different samples in Figure 3a, 3b ranging
162 from 6.5 m to 9 m. Many landslide sources have areas less than 100 m² (median mapped areas range from 42 m² to
163 64 m² for the different terranes), and very few have areas greater than 1000 m² (Fig. 3c). Although landslides occurred
164 on a wide range of slope angles, most occurred on slopes between 30° and 50° (Fig. 3d). Median DEM-derived slope
165 angles of mapped landslide sources were 37° - 39° (Fig. 3d). Depths computed by differencing pre-event and post-
166 event lidar elevation data (Baxstrom et al. 2021a; Einbund et al. 2021a, 2021b) have significant uncertainty because
167 14 - 19% of the landslide sources had mean and median elevation differences indicating net gain of material (Fig. 3e).
168 In addition, undisturbed areas outside the landslide polygons showed elevation differences that varied horizontally,
169 which is consistent with alignment errors between the pre- and post-event lidar. However, it seems unlikely that any
170 of the mapped landslides had a mean depth much greater than 5.8 m (the span between the greatest elevation loss and
171 gain, MVC/LAR2, Fig. 3e). Rare, large landslides had depths as great as 25 m according to field measurements (Fig.
172 3e).

173 Puerto Rico's complex geology (Fig. 1), tropical soils, rugged terrain, land use, and landcover exert strong influences
174 on landslide susceptibility. Lepore et al. (2012) in an island-wide assessment using frequency ratio and logistic
175 regression concluded that aspect, slope, elevation, geological discontinuities, and geology, were “highly significant
176 landslide-inducing factors;” land cover and distance from roads were also significant. Bessette-Kirton et al. (2019a)
177 showed that antecedent soil moisture was statistically correlated to densities of Hurricane-María-induced landslides
178 and found that high landslide densities were “especially widespread across some geologic formations,” although the
179 degree to which rainfall characteristics resulted in this correlation remained unclear. In a later post-Hurricane María,
180 island-wide assessment using the frequency ratio method, Hughes and Schulz (2020a) found after accounting for the
181 effects of soil moisture, there were strong correlations between landslides and slope, curvature, geologic terrane, mean
182 annual precipitation, land cover, soil type, event soil moisture, proximity to roads, and proximity to fluvial channels
183 for the Hurricane María event. Previous, more localized studies considered fewer geomorphic and geographic
184 characteristics to classify landslide susceptibility using empirical and statistical methods (Larsen and Parks 1998;
185 Larsen et al. 2004). For example, Larsen and Parks (1998) classified landslide susceptibility of Comerío Municipality
186 based on elevation, slope, aspect, and land use. Our current study uses physics based geotechnical models of slope
187 stability to directly assess topographic, geologic, and soil controls on landslide potential and to indirectly assess effects
188 of roads and land use through their impacts on topography and surface drainage as expressed in the DEM as local
189 changes in the slope characteristics.



190 3 Methods and materials

191 3.1 Topographic data

192 In 2015 and 2016, the U.S. Geological Survey (2018) acquired airborne lidar covering the entire main island of Puerto
193 Rico. These data were processed to create a 1-m resolution bare-earth DEM. Referred to hereafter as pre-event lidar,
194 these data were acquired roughly one to two years before Hurricane María and constitute the best available
195 representation of topographic conditions before the landslides associated with the hurricane occurred. Available at the
196 beginning of our investigation, the pre-event lidar-derived DEMs have formed the topographic mainstay for U.S.
197 Geological Survey studies of these recent landslides. We used these data for calibration and validation of our soil
198 depth and slope stability models. After Hurricane María, the U.S. Geological Survey (2020a, b, c) acquired additional
199 lidar data covering the entire island in 2018. These data, referred to hereafter as post-event lidar, constitute the
200 (currently) best available representation of topographic conditions after the landslides and are useful for assessing
201 susceptibility to future landslides. The 0.5-m post-event lidar DEMs were resampled to 1-m resolution for consistency
202 with the pre-event lidar and computational efficiency of landslide susceptibility models. We used these post-event
203 DEMs to run our models (using the previously calibrated and evaluated input parameters) to obtain our best estimate
204 of susceptibility to future landslides.

205 3.2 Data compilation

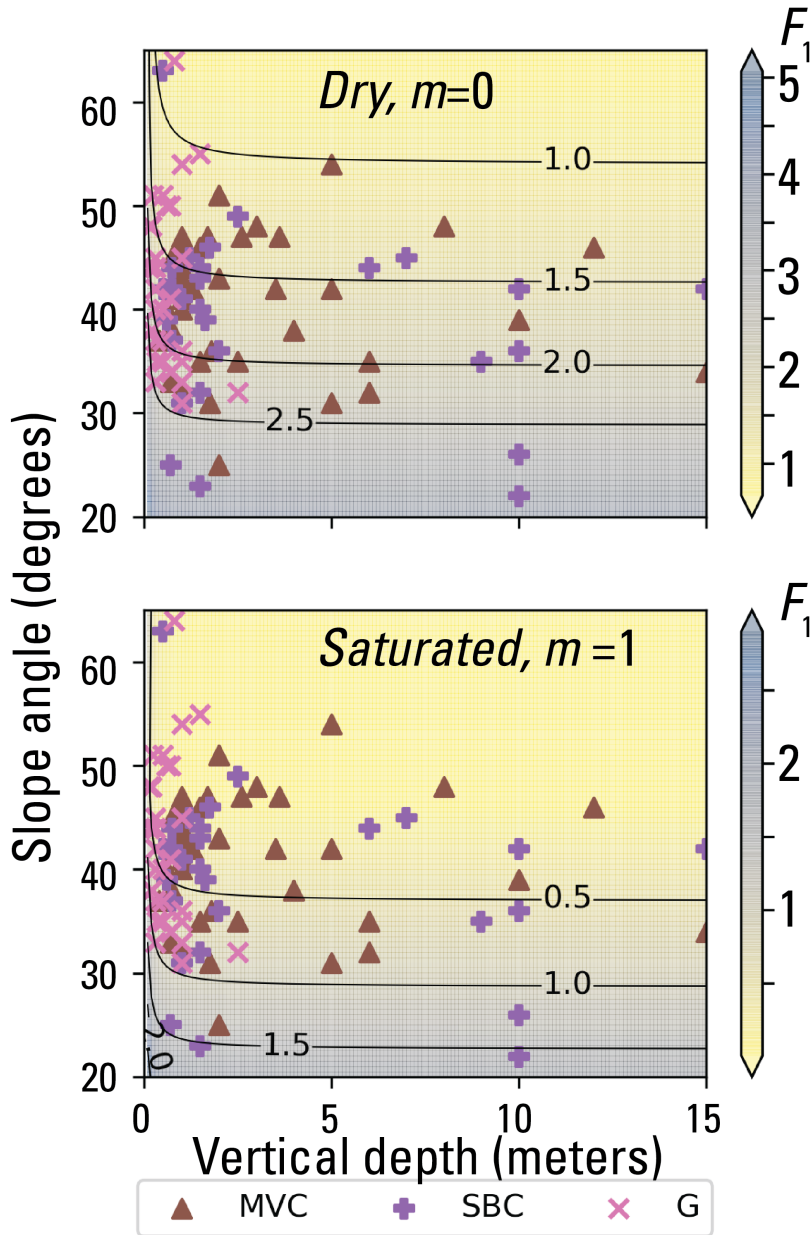
206 Based on findings by Bessette-Kirton et al. (2019a) and Hughes and Schulz (2020a, b) indicating strong correlation
207 between landslide density and both bedrock and soil type, Baum (2021) compiled existing data on soil texture and
208 engineering properties to create typical values for model calibration. Four different sources yielded soil and (or)
209 engineering data: published literature about past and recent landslides in Puerto Rico (Sowers 1971; Jibson 1989;
210 Simon et al. 1990; Larsen and Torres-Sanchez 1992, 1998; Lepore et al. 2013; Thomas and Cerovski-Darriau 2019),
211 NRCS soil databases (Soil Survey Staff; 2018), laboratory testing (Smith et al. 2020), and geotechnical reports of
212 recent landslides (Puerto Rico Department of Transportation, written commun. 2019). The NRCS soil data and
213 geotechnical reports were summarized in spreadsheets and then analyzed to determine means, ranges, and other basic
214 statistics to characterize the properties of soils and geologic formations found throughout the three municipalities
215 (Baum and Lewis, 2023). Baum (2021) identified dominant soil classes of the geologic terranes that had high landslide
216 densities (Fig. 1) and estimated expected ranges of soil strength parameters, cohesion, c' , and angle of internal friction,
217 ϕ' , both for effective stress based on dominant Unified Soil Classification System (ASTM International, 2020) types
218 in each terrane as follows: volcanoclastic, high-plasticity organic clay (OH), ϕ' $17^\circ - 33^\circ$, c' 5 – 20 kPa; submarine
219 basalt and chert, low plasticity clay (CL) and high-plasticity silt (MH), ϕ' $27^\circ - 35^\circ$, c' 5 – 20 kPa; granitoid, low
220 plasticity clay (CL) and silty sand (SM), ϕ' $27^\circ - 41^\circ$, c' 0 – 20 kPa.

221 3.3 Strength parameter analysis

222 Using 1D slope stability analysis, Baum (2021) estimated the ranges of soil strength parameters ϕ' and c' that explain
223 the largest number of field-observed landslide slope and depth combinations in the calibration areas (Fig. 4).



224 Computing 1D factor of safety, F_1 , for 1440 possible incremental combinations of ϕ' and c' over a synthetic grid in
225 which slope angle, δ , and landslide depth, H , varied incrementally over the observed ranges of slope ($22^\circ - 60^\circ$, in
226 0.5° increments) and depth (0.2 m – 15 m, in 0.1-m increments) produced F_1 values for more than 1.9×10^7
227 combinations of H , δ , ϕ' , and c' . The best fitting ranges (dark red in Fig. 5) included combinations of H , δ , ϕ' , and c' ,
228 where more than 75% of observed landslide scarp points were successfully predicted by $F_1 \geq 1$ for $\psi=0$ (dry, where ψ
229 is the pressure head at the basal slip surface) and $F_1 < 1$ for $\psi=H\cos^2\delta$ (water table at the ground surface with slope-
230 parallel flow). The example depicted in Fig. 4 had an overall success rate of 93% for its $c' - \phi'$ combination ($c' = 0.75$
231 kPa and $\phi' = 54^\circ$) in all three geologic terranes (Figs. 1, 5a). Compiling the performance of every $c' - \phi'$ pair considered
232 in the analysis led to Fig. 5b, 5c, and 5d, which showed the better-performing ranges of c' and ϕ' for the granitoid (Fig.
233 5b), volcanoclastic (Fig. 5c), and submarine basalt and chert (Fig. 5d) terranes, respectively. Those combinations of c'
234 and ϕ' with success rates exceeding 75%, were used as inputs for computing F_1 with trial soil-depth maps in subsequent
235 calibration studies to select a single combination of c' and ϕ' for computing F_1 in each terrane.
236



237

238

239

240

241

242

243

244

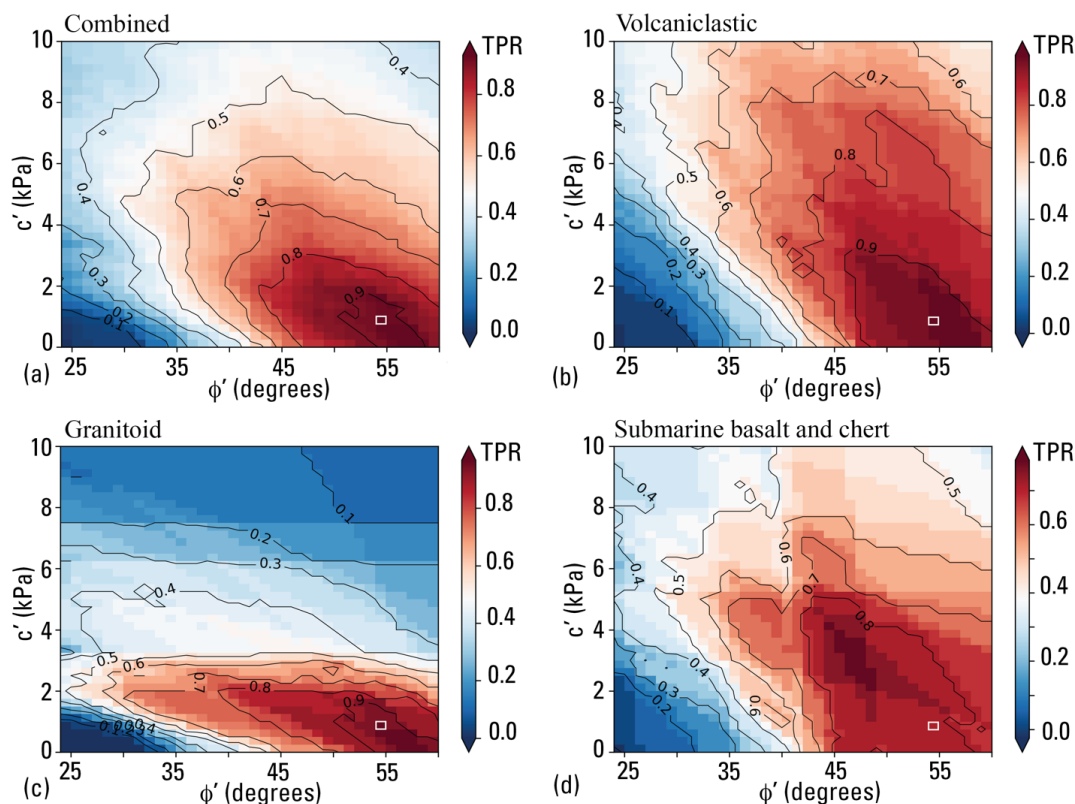
245

246

Figure 4. Results of strength parameter testing for observed combinations of landslide slope and depth in three geologic terranes. Factor of safety, F_1 , results (indicated by color scale and contour lines) for a selected combination of cohesion, c' ($c' = 0.75$ kPa) and angle of internal friction, ϕ' ($\phi' = 54^\circ$), both for effective stress. Two scenarios for pore-pressure head ($m=0$ and $m=1$) are shown, where m is the ratio of pressure head to soil depth. Symbols mark observed slope angle and depth at mapped landslide sources in various geologic terranes (Fig. 1). Factor of safety, F_1 , at slope and depth combinations observed at marked landslide sources indicates model success ($F_1 < 1$ if $m=1$) or failure ($F_1 > 1$ if $m=1$). For the pair of c' and ϕ' values shown, $F_1 > 1$ for dry conditions ($m=0$) at about 97% of sources and $F_1 > 1$ at 4% of sources for water table at the ground surface with flow parallel to the slope ($m=1$). These parameters, $c' = 0.75$ kPa and $\phi' = 54^\circ$, had an overall success rate of about 93% (=97% - 4%) for all three terranes (revised from Baum 2021).



247



248

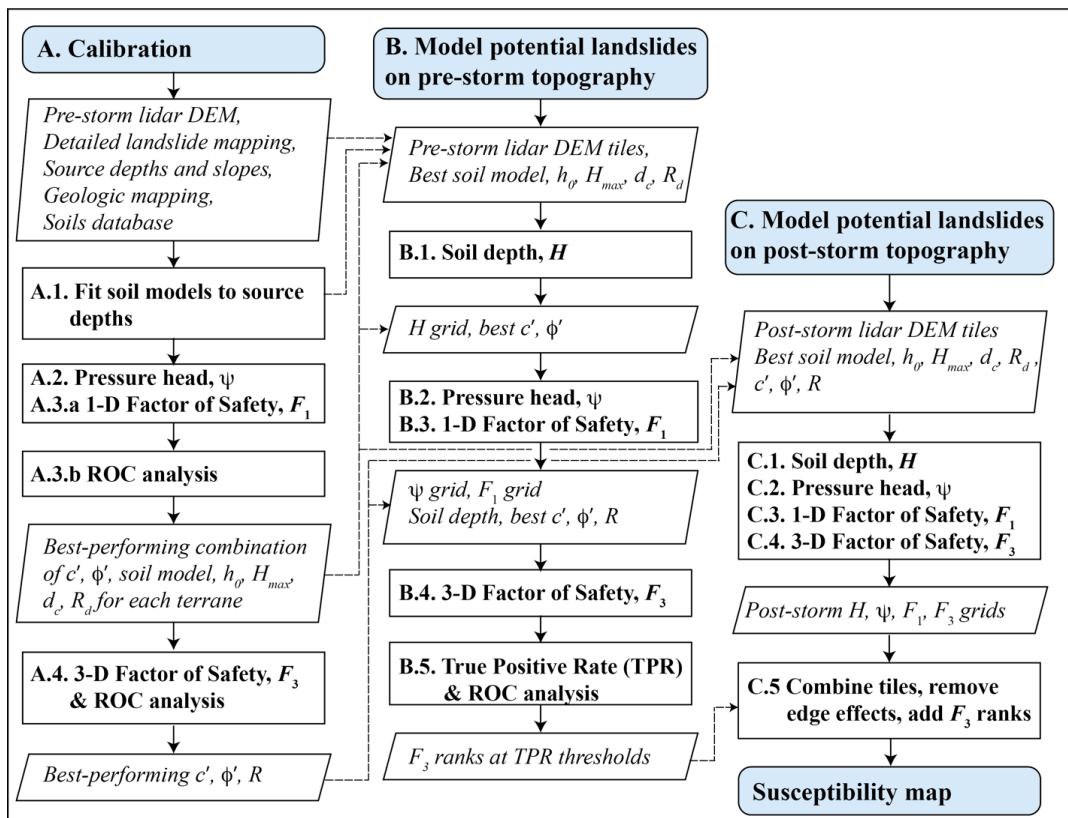
249 **Figure 5.** Fraction of field-measured landslide sources from the calibration areas (Baum et al. 2018) predicted correctly as
 250 a function of cohesion, c' , and angle of internal friction, ϕ' , for observed landslides in (a) all three terranes combined
 251 (modified from Baum 2021); (b) the volcaniclastic terrane; (c) the granitoid terrane; (d) the submarine basalt and chert
 252 terrane. Each pixel summarizes the net result of a pair of analyses like that in Figure 4. Pixel outlined by white rectangle in
 253 lower right corner of panels (a), (b), (c), and (d) indicates combination for analysis shown in Figure 4. Pixel color and
 254 contours indicate true positive rate (TPR) of predictions for each cell. Factor of safety for dry conditions is $F_{1m=0}$; factor of
 255 safety for water table at ground surface with slope-parallel flow is $F_{1m=1}$. Each grid cell represents the fraction $(NF_{1m=0} -$
 256 $NF_{1m=1})/N_t$, where $NF_{1m=0}$ is the number of source areas for $F_1 \geq 1$, $NF_{1m=1}$ is the number of source areas for which $F_1 \geq 1$,
 257 and N_t is the number of source areas in the geologic terrane.

258 3.4 Workflow for shallow landslide susceptibility models

259 To represent the aerial extent and depths of potential landslide source areas, we undertook a multistage process to
 260 calibrate and model potential landslide sources for both pre-Hurricane María and post-Hurricane María digital
 261 topography (Fig. 6). Each stage (depicted as a column in Fig. 6) repeated four distinct modelling steps: (1) soil depth,
 262 H , (2) pressure head, ψ , (3) 1D factor of safety, F_1 , (4) quasi-3D factor of safety, F_3 . The landscapes of the calibration
 263 and study areas were represented digitally in the models as raster grids based on 1-m-resolution pre-event lidar-derived
 264 DEMs. Each grid cell represented a column of potential landslide material of vertical depth, H , determined at soil-
 265 depth modelling steps A.1, B.1, and C.1 (Fig. 6). Computed soil depth from these steps became input for calculation
 266 of ψ , (steps A.2, B.2, and C.2, respectively, Fig. 6); then H and ψ became inputs for computing F_1 (steps A.3.a, B.3,



267 and C.3, Fig. 6) and F_3 (steps A.4, B.4, and C.4, Fig. 6). F_1 was used primarily in evaluating soil-depth models and
 268 shear-strength parameters for the calibration areas depicted in Fig. 1 using receiver operating characteristic (ROC)
 269 analysis (step A.3.b, Fig. 6). During post-calibration slope-stability modelling of the study areas (steps B.4 and C.4,
 270 Fig. 6), F_1 served as a rough check on the computed value of F_3 . In this section (Sect. 3.4.1, 3.4.2, 3.4.3, and 3.4.4),
 271 we briefly describe the modelling steps and give details about the models. We describe the major stages (columns in
 272 Fig. 6) of calibration, modelling, and validation in later sections (Sect. 3.5, ..., 3.11).
 273



274
 275 **Figure 6.** Flow chart showing major stages (each column) and steps of calibration and modeling leading to the map of
 276 landslide initiation susceptibility (Susceptibility map, bottom of right column). The calibration stage (left column) was
 277 performed using digital elevation models of roughly 2.5-km² areas where detailed mapping and fieldwork had been
 278 conducted (Fig. 1). Landslide source depths approximated soil depth for soil-depth model calibration (1.1). The pre-
 279 Hurricane Maria (pre-storm) modeling stage (center column) was conducted using overlapping DEM files (Fig. 1) derived
 280 from pre-Hurricane Maria lidar (U.S. Geological Survey, 2018). The post-Hurricane Maria (post-storm) modeling stage
 281 (for generating map of future landslide susceptibility, right column) used overlapping DEM tiles (Fig. 1) derived from post-
 282 Hurricane Maria lidar (U.S. Geological Survey, 2020a, b, c). Post-Hurricane Maria steps 3.1, 3.2, 3.3, and 3.4 used identical
 283 input parameters to the corresponding pre-Hurricane Maria steps, 2.1, 2.2, 2.3, and 2.4. [Chart symbols: Light-blue
 284 rounded rectangles, terminals of each major stage; rectangles with bold text, computational processes; parallelograms with
 285 italic text, inputs or outputs; dashed lines, connections between calibration outputs and model inputs. Model outputs: H ,
 286 soil depth; ψ , pressure head; F_1 , 1D factor of safety; F_3 , quasi-3D factor of safety; TPR, true positive rate; ROC, Receiver
 287 Operating Characteristics. Model input parameters: h_0 , characteristic soil depth, H_{max} , maximum soil depth; d_c , critical
 288 slope angle; R_d , diffusivity ratio; c' , cohesion for effective stress; ϕ' , angle of internal friction for effective stress; R , radius
 289 of quasi-3D trial surface.]



290 3.4.1 Step 1, modelling soil depth

291 Estimating soil depth from a DEM was the first modelling step in all three stages (Fig. 6). Field observations indicated
292 that the base of most landslide sources occurred near the top of weathered bedrock (Baum et al. 2018; Baum 2021),
293 so we chose soil depth as a predictor of landslide source depth. We carried out soil-depth estimation using new open-
294 source software, REGOLITH (Baum et al. 2021) containing five empirical and four steady-state process-based soil-
295 depth models implemented in a command-line program. Each model in REGOLITH estimates soil depth from some
296 combination of topographic variables, including slope, upslope contributing area, and curvature, as well as a few
297 model parameters, such as characteristic depth (the soil thickness at which bedrock lowering falls to 1/e of its
298 maximum value), h_0 [L]; critical slope (angle of stability at which the slope is capable of transporting the entire soil
299 profile by mass movement), δ_c [degrees]; and the ratio of maximum bedrock lowering rate to hillslope diffusivity, R_d .
300 These parameters may vary with conditions that influence soil formation, including bedrock and climate. Predicted
301 soil depth is treated as equivalent to and defines column height, H , in subsequent modelling steps. We used separate
302 property zones with distinct parameters in REGOLITH to model adjoining areas of significantly different soil depth
303 characteristics (tropical karst versus granitoid and volcanoclastic). We modified steady-state process-based models
304 (Pelletier and Rasmussen 2009), which predict soil depth only on convex topography, to estimate soil depths in both
305 concave and convex topography. We used a smoothing algorithm available in REGOLITH to reduce abrupt changes
306 in soil depth that may result from DEM roughness. Further details are available in the online documentation found in
307 the code repository (Baum et al. 2021). Our soil-depth, pressure head, and slope-stability models treated roads, cut
308 slopes and embankments the same as other areas.

309 3.4.2 Step 2, modelling subsurface pressure head

310 Step 2 was performed using the Transient Rainfall Infiltration and Grid-Based Regional Slope-Stability Analysis
311 (TRIGRS) program (Baum et al. 2010; Alvioli and Baum 2016), version 2.1. In most applications, TRIGRS computes
312 pressure head and factor of safety distributed over a digital landscape to yield a series of grids representing changes
313 in pressure head and factor of safety through time during a rainfall event. For this work, our objective was a landslide
314 susceptibility map that shows where landslides induced by intense rainfall are most likely, so we used a presumed
315 wettest-case pressure head, rather than simulating time-varying pressure head. This approach greatly accelerated the
316 Step 2 pressure-head computations and eliminated the need to calibrate soil hydraulic parameters. Given the extreme
317 rainfall during Hurricane María and other historical tropical storms, full saturation with the water table at the ground
318 surface and groundwater flow sub-parallel to the ground surface (as determined by the permeability contrast at the
319 soil-saprolite or soil-bedrock boundary) represented the likely wettest-case hydrologic conditions for landslide
320 initiation. This approach neglects effects of suction stress, heterogeneity, and transient pore pressures at the cost of
321 making the susceptibility map more conservative (more false positives). Thus, for this assessment we estimated
322 pressure head for these conditions using the following steady-state formula (Iverson 2000; Baum et al. 2010):

$$323 \psi(Z) = (Z - d) \left[(\cos \delta)^2 - \frac{lZLT}{K_s} \right] \quad (1)$$



324 In Eq. (1), $\psi(Z)$ [L] is the pressure head as a function of Z [L], the vertical coordinate direction (positive downward
325 from the ground surface); d [L] is the steady-state depth to the water table measured in the vertical direction (0 m in
326 this case); I_{ZLT} [LT^{-1}] is the steady background flux; δ is the slope angle; and K_s [LT^{-1}] is the saturated hydraulic
327 conductivity. The dimensionless ratio I_{ZLT}/K_s in Eq. (1) accounts for downward percolation and reduces the pressure
328 head from the slope parallel case represented by $H\cos^2\delta$, where $H (=Z-d)$ is the column height as noted previously.
329 The average rate of downward percolation is strongly controlled by the permeability contrast between the mobile
330 regolith (soil mantle) and underlying weathered bedrock or saprolite. For the problem considered here, $I_{ZLT}/K_s = 0.028$,
331 consistent with wet initial conditions (averaging 2-25 mm/day of precipitation-induced infiltration, I_{ZLT} , for K_s in the
332 range $10^{-5} - 10^{-6}$ m/s, typical of soils in the study area). This value of I_{ZLT}/K_s directs flow slightly downward and
333 reduces the pressure head by less than 1% compared to slope-parallel flow in the $25^\circ - 55^\circ$ range of slopes where most
334 landslides occurred. TRIGRS computes $\psi(Z)$ for a series of equally spaced depths between the ground surface ($Z=0$)
335 and a user-specified maximum depth, $Z=Z_{max}$. For this analysis, $Z_{max} = H$ as determined by the soil depth modeled in
336 stage A and we used a depth increment of $Z_{max}/10$.

337 3.4.3 Step 3, 1D factor of safety

338 TRIGRS computes the 1D factor of safety, F_1 , using the infinite slope analysis (Taylor 1948; Iverson 2000) according
339 to the following formula for the saturated case:

$$340 \quad F_1 = \frac{\tan \phi'}{\tan \delta} + \frac{c' - \psi(Z)\gamma_w \tan \phi'}{Z\gamma_s \sin \delta \cos \delta} \quad (2)$$

341 In Eq. (2) γ_s is the saturated unit weight of soil; γ_w is the unit weight of water; and δ is the true dip of the slip surface
342 at the base of mobile regolith (assumed parallel to the slope of the ground surface in the infinite slope analysis).
343 TRIGRS computes F_1 at the same series of depths between the ground surface and modeled soil depth as for $\psi(Z)$.
344 Eq. (2) is strictly valid for landslides much longer than their depth on planar slopes in which lateral variation in stress
345 is negligible. With the advent of high-resolution topography, the depth-to-length ratios of soil columns at most grid
346 cells have become much greater than 0.1, such that the small depth-to-length landslide assumption of Eq. (2) is
347 violated. This violation reduces accuracy for nonplanar slopes and for rough DEMs (whether the roughness results
348 from natural surface roughness or from data collection and processing errors). A slope-stability analysis that considers
349 multiple adjacent DEM cells can improve accuracy for nonplanar slopes and rough DEMs.

350 3.4.4 Step 4, 3D factor of safety

351 To overcome the limitations of F_1 for high-resolution topography and to assess the stability of potential source areas
352 similar in size to past landslides, the computed pressure head, Eq. (2), was used in a separate computer program,
353 Slabs3D (Baum 2023), to compute the quasi-3D factor of safety, F_3 . Baum et al. (2012) described and tested a
354 preliminary version of the program, which recently was further developed and tested for the work reported here.
355 Slabs3D was designed to rapidly analyze stability of the soil mantle on hillsides to identify potential shallow landslide
356 sources. By using a method of columns, Slabs3D overcomes some of the limitations of infinite-slope computations on
357 high-resolution topography. However, the current version of Slabs3D relies on force equilibrium alone (not moment



358 equilibrium). Thus, the approximations made in computing F_3 are suitable only for thin (disc- or slab-shaped)
359 landslides, such as most landslides in the study areas (Figs. 2, 3). Potential landslides can be more thoroughly analyzed
360 with 3D slope-stability software such as Scoops3D, which considers moment equilibrium on arcuate trial surfaces
361 (Reid et al. 2015). However, in consideration of the thin, slab-shaped landslide sources and the large area (about 1000
362 km²) to be analyzed, we deemed the accuracy of Slabs3D sufficient and its speed to outweigh any potential
363 improvements in accuracy offered by Scoops3D. Slabs3D computes F_3 as follows (Hovland, 1977):

$$364 \quad F_3 = \frac{\sum[(H\gamma_s - \psi\gamma_w)\ell_x\ell_y \cos \delta \tan \phi' + c'A]}{\sum H\gamma_s\ell_x\ell_y \sin \delta_a} \quad (3)$$

365 In Eq. (3), the sums are taken over all the columns within the potential landslide. The quantities ℓ_x and ℓ_y are the
366 horizontal grid cell dimensions; the column height, H , is taken as the modeled soil depth from Step 1; δ_a is the apparent
367 dip of the basal slip surface, $b=b(x, y)$, along the (assumed) direction of sliding. A is the true area of the failure surface
368 at the base of the column (Hovland 1977; Hungr et al. 1989):

$$369 \quad A = \ell_x\ell_y \sqrt{1 + \left(\frac{\partial b}{\partial x}\right)^2 + \left(\frac{\partial b}{\partial y}\right)^2} \quad (4)$$

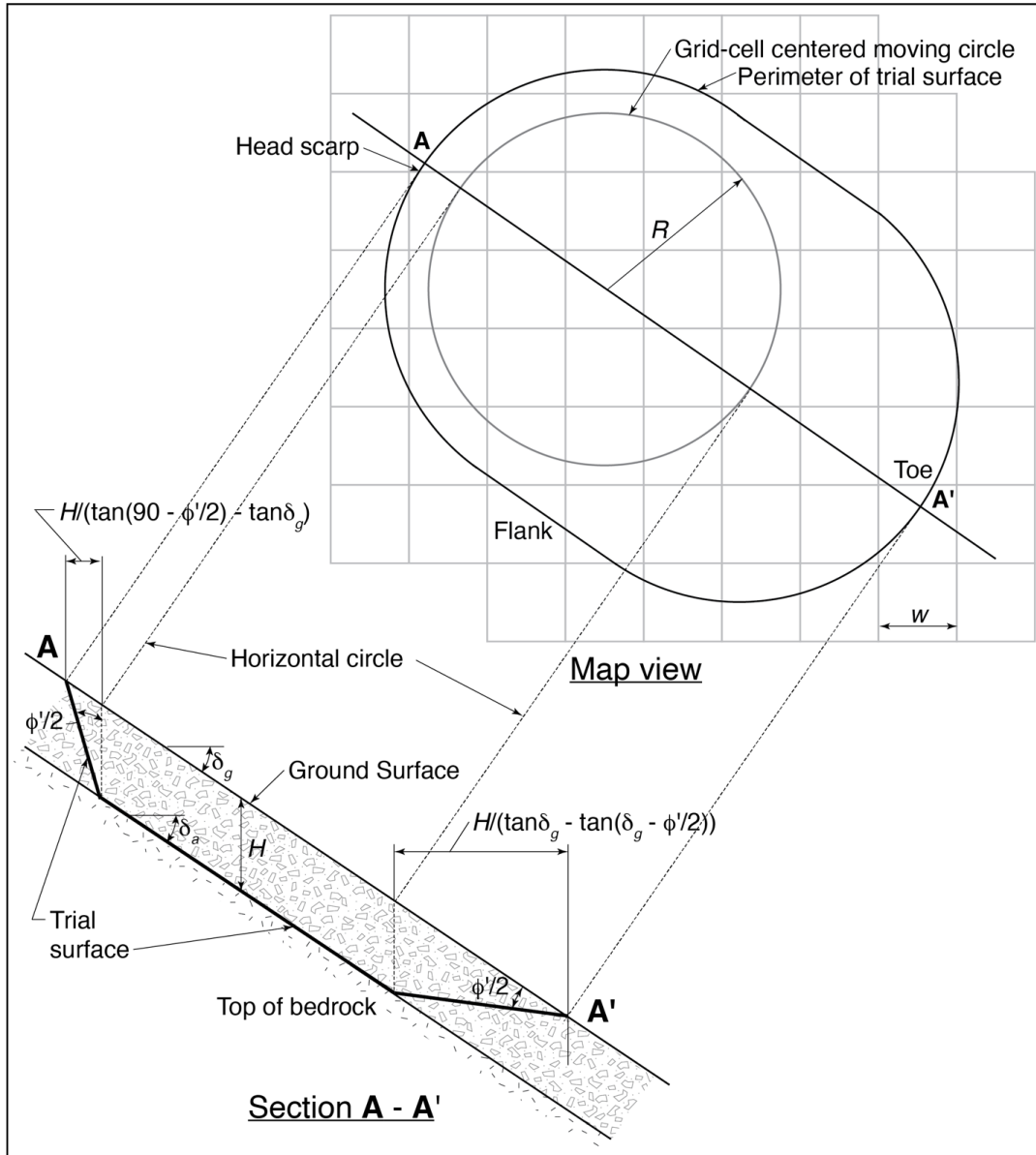
370 The choice to take H as the modeled soil depth at each grid cell in Eq. (3) is consistent with field observations and
371 previous modelling results. As noted previously, our field observations indicated that the base of most landslide
372 sources occurred directly above a strength and permeability contrast. Except for cases of very rapid infiltration,
373 TRIGRS computes the lowest factor of safety at Z_{max} . Smoothing the modeled soil depth reduces potential irregularities
374 in the trial surface. Tests indicated that modest irregularities have only minor effect on F_3 (Baum, 2023).

375 In Eq. (3), the effect of pore pressure has been computed in a manner consistent with the normal application of the
376 principle of effective stress by subtracting the pore pressure or suction stress from the gravity-induced stress rather
377 than computing the resultants of pore pressure and gravity stress acting normal to the trial failure surface separately
378 as in some implementations of the ordinary method of slices (Turnbull and Hvorslev 1967). Despite its limitations,
379 Hovland's (1977) method of columns is always able to compute a factor of safety and is not subject to the convergence
380 problems that occasionally occur with more sophisticated limit-equilibrium methods.

381 As noted previously in the 1D analysis, Eq. (2) computes F_1 at each grid cell for a range of depths from the ground
382 surface down to a user-specified maximum depth, which in this case is the computed soil depth, H , from step B.1
383 (Baum et al. 2008, 2010). For the cases tested here, the minimum F_1 always occurred at the base of soil, so we limited
384 our search for 3D potential failures to those that follow the base of soil. In computing F_3 , we searched the entire digital
385 elevation model (DEM) for potential failures to a maximum depth of H using a circle of fixed diameter (in map view)
386 centered at each grid cell to define the base of potential failure surfaces (one per grid cell, Fig. 7). Average dip direction
387 of the base of soil within the circle determined the assumed slip direction. Potential failure surfaces enclosed by partial
388 circles near the edges of the DEM were excluded from the analysis. Consequently, we extended the DEM grid well
389 beyond the area needed for the final susceptibility map so that any inaccurate F_3 values near the DEM grid boundaries
390 could be discarded as described in the Sect. 3.10, "Removing edge effects." This approach of using map-view-circular
391 trial failure surfaces resulted in potential landslides having the shape of an oblong slab or disc of variable thickness
392 with tapered edges and rounded ends (Fig. 7), such that the trial surface was shaped somewhat like a gold pan. Beyond
393 the limits of the search circle, the slab thins as the potential failure surface slopes from the approximate base of soil



394 toward the ground surface. The failure surface at the head and flanks of the potential slides was assumed (based on
395 Rankine theory, Lambe and Whitman 1969; Terzaghi et al. 1996) to slope $90^\circ - \phi/2$ and beneath the toe to slope $\delta_g -$
396 $\phi/2$ (where δ_g is the slope of the ground surface) from the ground surface down to the edge of the circle (Fig. 7). We
397 estimated the contributions of wedges of material at the head, toe, and sides to total driving and resisting force by
398 substituting formulas for height, length, width, average pressure head, and basal area (H , ℓ_x , ℓ_y , ψ , and A) of each side
399 wedge, into Eq. (3) (Fig. 7), rather than subdividing the wedges into their component square columns or partial
400 columns and summing their individual contributions. The size of these wedges is negligible with a grid resolution
401 greater than the depth, H , as is often the case for our study areas, with soil depth commonly less than the 1-m resolution
402 of our DEM. The wedge formulas are exact only for constant H . Although variable H across the trial surface introduces
403 minor uncertainty into F_3 , the formulas are sufficiently accurate for estimating the value of F_3 for assessing stability
404 of the soil mantle over large areas.



405

406

407

408

409

410

411

412

413

414

415

416

Figure 7. Sketch showing moving circle search strategy and trial surface geometry used in computing approximate 3D factor of safety, F_3 . All grid cells whose center is inside the circle are included in the computation of F_3 , and cells in the head scarp, flank, and toe areas are combined to form wedges for computational purposes. The trial surface has a map-view radius R ; δ_g is the slope of the ground surface; δ_a is the apparent dip of the trial surface in the assumed direction of sliding (average slope direction of grid cells centered within the horizontal circle); H is height of a grid-cell centered column from the trial surface to the ground surface; and ϕ' is the angle of internal friction of the soil for effective stress (modified from Baum et al. 2012). For the case depicted in Section A-A' (above), H is constant and 1.5 times the horizontal width, w , of the square grid cells. As the average value of H/w decreases and as R increases, the perimeter of the trial surface contracts toward the projection of the horizontal circle onto the ground surface. For variable soil-depth models, H may vary from cell to cell and the value of H for the grid cell closest to the upslope or downslope edge of the horizontal circle is used in the formulas shown in the cross section for horizontal dimensions of the scarp and toe respectively.



417 3.5 Soil-depth model calibration

418 Soil-depth model calibration proceeded first by fitting soil models to depth observations followed by checking how
419 the best-fitting models performed as input for computing F_1 to predict landslide locations (see Sect. 3.6). Both
420 calibration and checking made use of pre-event 1-m bare-earth lidar digital elevation models for the four ~2-km²
421 calibration areas representing the dominant (three) geologic terranes affected by landslides in the study areas (Fig. 1).
422 Landslides had previously been mapped (Bessette-Kirton et al. 2019c) and characterized (Baum et al. 2018) in these
423 four calibration areas (Sec. 2.2, Fig. 3). Tello (2020) described the soil-depth calibration procedures in detail. We
424 summarize important steps here: Field-measured landslide scars on unmodified hillsides (no obvious cut or fill) served
425 as calibration points for soil depth. Tello (2020) adjusted GPS location of each calibration point to the center of its
426 corresponding landslide polygon mapped from imagery by Bessette-Kirton et al. (2019c). A 5-m buffer around each
427 point ensured adequate sampling of model depths to be compared with the field-measured maximum depth. Tello
428 (2020) used a provisional version of the soil-depth code, REGOLITH (Baum et al. 2021), to model trial soil-depth
429 distributions for the calibration areas. Multiple runs to incrementally sample the parameter spaces of several different
430 soil models implemented in REGOLITH produced hundreds of trial soil depth grids for each of the four calibration
431 areas. Soil models tested include a linear area- and slope-dependent model (LASD) (Ho et al. 2012) and modified
432 forms of Pelletier and Rasmussen's (2009) non-linear slope- (NSD), area- and slope- (NASD), and slope- and depth-
433 dependent (NDS) models. Testing these against the field-measured landslide-scar maximum depths resulted in
434 optimized input parameters for each model and area (Tello 2020).

435 Tello (2020) used a range of statistical metrics identified by Gupta et al. (2009) to determine predictive success of the
436 model outputs. Most important of these was the Euclidian distance from the ideal point, ED . The ideal point is
437 characterized by perfect correlation between observed and simulated points and by perfect agreement between the
438 means and standard deviations of the observed and simulated point distributions,

$$439 \quad ED = \sqrt{(r - 1)^2 + (\alpha - 1)^2 + (\beta - 1)^2} \quad (5)$$

440 where the ideal point is at $r=1$, $\alpha=1$, $\beta=1$ so that $ED=0$. The linear correlation coefficient, r , relative variability, α , and
441 the bias relative to the observed sample, β , define the ED in eq. (5) (Gupta et al. 2009). In eq. (5) the relative variability
442 is the ratio of the standard deviation of the simulated values, σ_s , to the standard deviation of the observed values, σ_o ,
443 ($\alpha=\sigma_s/\sigma_o$). Likewise, the bias is the ratio of mean of the simulated values, μ_s , to the mean of the observed values, μ_o ,
444 ($\beta=\mu_s/\mu_o$). The linear correlation coefficient, r , indicates the quality of a least-squares fit of the simulated values to the
445 observed values, with $r=1$ indicating a perfect fit. The model run having the lowest ED usually had the best fit, unless
446 $ED > 1$ (Tello 2020). Where $ED > 1$, we chose the model run with β closest to 1 so that the mean simulated depth would
447 be as close as possible to the mean of depth observations (Gupta et al. 2009). The best-fit soil-depth distribution
448 corresponded in turn to a best-fit parameter set for each soil-depth model type. Comparison of best scores for each
449 model type identified the overall best fit of all models tested.



450 3.6 Soil model evaluation and slope-stability calibration

451 To further evaluate the soil-depth modelling results and finish calibrating the slope-stability model, we computed F_1
452 for dry and saturated soil conditions using the better performing soil-depth models for each calibration area. Previously
453 defined better performing (TPR $\geq 75\%$) ranges of ϕ' and c' (Baum 2021; Fig. 5b, 5c, 5d) defined the parameter space
454 for computing F_1 with a well-performing subset of trial soil-depth distributions. In addition, we required $F_1 > 1$ in
455 99.9% of grid cells for $\psi(H)=0$ to ensure slope stability under dry conditions. Computing F_1 over the calibration areas
456 using the best-fit distributions for each soil-depth model type and ϕ' and c' combinations produced many F_1 grids.
457 Receiver Operator Characteristics (ROC) analysis (Fawcett 2006, Pegueria 2006) of these F_1 grids against mapped
458 landslide scarp points indicated which combinations of trial soil-depth distribution and strength parameters predicted
459 the most observed landslides, based on the area under the ROC curve. Using parameters from the highest performing
460 F_1 distribution, we selected the preferred soil depth model and ϕ' and c' values for modelling F_1 in the large study
461 areas enclosing Lares, Utuado, and Naranjito municipalities. The calibration areas represented different geologic
462 terranes having the highest densities of landslides in the study areas so that the calibration procedure yielded separate
463 model and parameter values relevant to each of these terranes.

464 After H and F_1 values had been improved as much as possible by calibration, we began test calculations of F_3 and
465 worked to further refine potential landslide source areas. We varied the size of the trial surface from a 3.5-m radius to
466 a 10.5-m radius (Fig. 7) and used ROC analysis along with information about observed source-area sizes to determine
467 the optimum F_3 radius. Due to insufficient data, rigorous calibration was not possible for some parameter zones, such
468 as the karst areas of Bawiec's (1998) Limey sediment terrane. We adjusted model parameters (reduced maximum soil
469 depth, H_{max} , and characteristic soil depth, h_0 , for the soil-depth model and increased c' for computing F_1 and F_3) for
470 the Limey sediment terrane's parameter zone to account for the terrane's low landslide density during Hurricane María.

471 3.7 Geologic mapping and parameter zonation

472 Bawiec (1998) compiled published 1:20,000-scale geologic mapping of Puerto Rico and (as noted previously)
473 combined related formations into geologic terranes (Fig. 1 and Bawiec 1998). Based on the results of early studies
474 (Bessette-Kirton et al. 2019a) and our calibration efforts, the geologic terranes became the basis for subdividing the
475 study areas into parameter zones. The topographic base maps available at the time of geologic mapping lacked the
476 detail of the pre-event lidar-derived topography used in this study. Trial computations of F_1 and F_3 on the study area
477 DEM tiles indicated that a uniform soil depth model across the highly susceptible geologic terranes resulted in a more
478 accurate susceptibility map than a zoned model using the calibrated soil depth parameters. Uniform values of ϕ' and
479 c' for the highly susceptible geologic terranes likewise resulted in good performance so we used the same soil depth
480 and strength parameters for all three terranes (Supplemental Figures S1 and S2). Consequently, slight uncertainty in
481 locations of boundaries between these terranes had no effect on computed F_1 and F_3 values. However, a large
482 difference in landslide susceptibility and model parameters (maximum soil depth, h_0 , c') existed between the Limey
483 sediment terrane with its cone karst and the highly susceptible terranes of the basement complex (submarine basalt,
484 volcanoclastic, and granitoid). Offsets as great as tens of meters in the contact between the Limey sediment terrane
485 and its neighbors along a prominent escarpment in Lares and Utuado resulted in errors in F_1 and F_3 along the



486 escarpment. Consequently, Perkins et al. (2022) remapped the Limey sediment contact using lidar-derived shaded
487 relief images and optical imagery to accurately delineate the transition from high to low landslide susceptibility across
488 the contact. The contact was discerned based on the visually distinct differences between the closed basins and rugged
489 karst cones of the Limey sediment terrane and the steep ridges and narrow branching valleys of the basement rocks.

490 **3.8 Soil-depth modelling**

491 After completing the calibration process, we created the overlapping rectangular tiles (described previously, Sec. 1.0,
492 3.1) from the pre-event lidar bare-earth DEMs (Fig. 6, stage B and Fig. 1b, 1c). We created additional input files from
493 the lidar-derived DEM tiles: flow accumulation grids for use with the area-dependent soil-depth models and
494 parameter-zone grids for specifying different model input parameters (Sec. 3.6, 3.7 and step B.1, Fig. 6). The
495 parameter zones ensured a thinner and less continuous modeled soil mantle in the karst (Limey sediment terrane) than
496 in areas underlain by the landslide-prone geologic terranes (Fig. 1).

497 **3.9 Pressure-head and slope-stability modelling**

498 Raster grids created from the soil-depth modelling defined soil depth (H) and slope of the ground surface at each grid
499 cell in TRIGRS. We computed ψ and F_1 using TRIGRS as described previously using the same lidar-derived DEM
500 tiles and parameter zones as for soil-depth modelling (steps B.2 and B.3, Fig. 6). Then, using $\psi(H)$ computed with
501 TRIGRS along with the same lidar tiles, parameter zones, and ϕ' and c' values used in computing F_1 as input for
502 Slabs3D, we computed F_3 (step B.4, Fig. 6). The radius of each trial surface, as constrained by earlier testing in the
503 calibration areas (Sect. 3.6, 4.5), was held constant at 3.5 m for all model runs on study area tiles.

504 After modelling potential source areas on pre-event topography, we recomputed the models using post-event 1-m lidar
505 topography (U.S. Geological Survey, 2020a, b, c). We generated new slope, zone, and flow-accumulation grids from
506 the post-event lidar and then ran REGOLITH, TRIGRS, and Slabs3D in succession (Fig. 6, steps C.1, C.2, C.3, and
507 C.4) to indicate our best estimate of susceptibility to future landslide initiation.

508 **3.10 Removing edge effects**

509 To reduce edge effects (Fig. 6, step C.5) when joining the four overlapping tiles for Lares and Utuado to create a final
510 map (based on post-event lidar), we first removed a 100-m buffer along all edges of each tile. At grid cells where two
511 tiles overlapped, differences in F_3 tended to be small and we retained the greater F_3 value. For the single tile covering
512 Naranjito, we removed only the 100-m buffer along all tile edges.

513 **3.11 Model testing and evaluation**

514 We used ROC analysis of F_3 grids based on pre-event lidar topographic data compared to landslide head-scarp points
515 mapped by Hughes et al. (2019) as a basis for testing performance and then defining susceptibility categories (step
516 B.5, Fig. 6). Selecting the minimum F_3 value within a 3-m radius around the scarp points accounted for uncertainty in
517 their mapped locations. Validating F_3 for pre-event topography was appropriate because it most accurately portrayed
518 conditions at the time of Hurricane María. We computed true positive rate (TPR), false positive rate (FPR), and area



519 under the TPR-FPR curve (AUC) and **distance from the ideal point** (d_{IP}), (0,1), to evaluate performance of pre-event
520 F_3 as a predictor of observed landslide scarp points. Analyzing landslide density distribution across F_3 provided a
521 further check on model accuracy. We computed landslide densities in 0.1 increments of F_3 to check for a general trend
522 of decreasing observed density with increasing F_3 . In addition to these quantitative assessments, we inspected the
523 maps to confirm that the susceptibility zones and potential source areas made sense topographically, mechanically,
524 and geologically. These inspections helped ensure that potential landslide source areas were consistent with
525 observations and expectations for hillsides whether they were relatively undisturbed or modified by roads, cut slopes,
526 and embankments. The inspections led to some minor revisions of the computer code to correct errors, followed by
527 repeated model runs.

528

529 As an additional check we computed ROC statistics for minimum F_3 values within source areas mapped by Baxstrom
530 et al. (2021a) and Einbund et al. (2021a, 2021b). Their detailed landslide source mapping covers only a fraction of the
531 study areas (Fig. 1), whereas the scarp points mapped by Hughes et al. (2019) cover the entire island. However, source
532 area polygons enclose pixels that are more relevant to testing performance of F_3 than circles centered at the scarp
533 points.

534 **Evaluating the model to address the need for a conservative landslide susceptibility map led us to select threshold**
535 **values of F_3 enclosing specific percentages (or TPR) of landslide points.** Every F_3 contour on the map encloses a
536 specific percentage of landslide points. Contours at high F_3 values enclose more landslide points than low F_3 contours.
537 We selected F_3 contours corresponding to TPR of 0.75 and 0.90 of Hurricane Maria-produced landslide head-scarp
538 points (Hughes et al. 2019) to define the limits of very high (TPR \leq 0.75), high (0.75 \leq TPR \leq 0.90), and moderate
539 (TPR $>$ 0.90) landslide source susceptibility zones. These classes include most mapped landslide points as well as the
540 adjacent steep slopes where they occurred, while limiting the overall areal extent of the very high and high
541 susceptibility classes. Using the same F_3 thresholds at TPR \leq 0.75 and TPR \leq 0.90 determined for the pre-event
542 topography (step B.5, Fig. 6), we then defined landslide susceptibility zones using post-event topography across the
543 three municipalities (step C.5, Fig. 6). These zones estimate the potential for future shallow landslides.

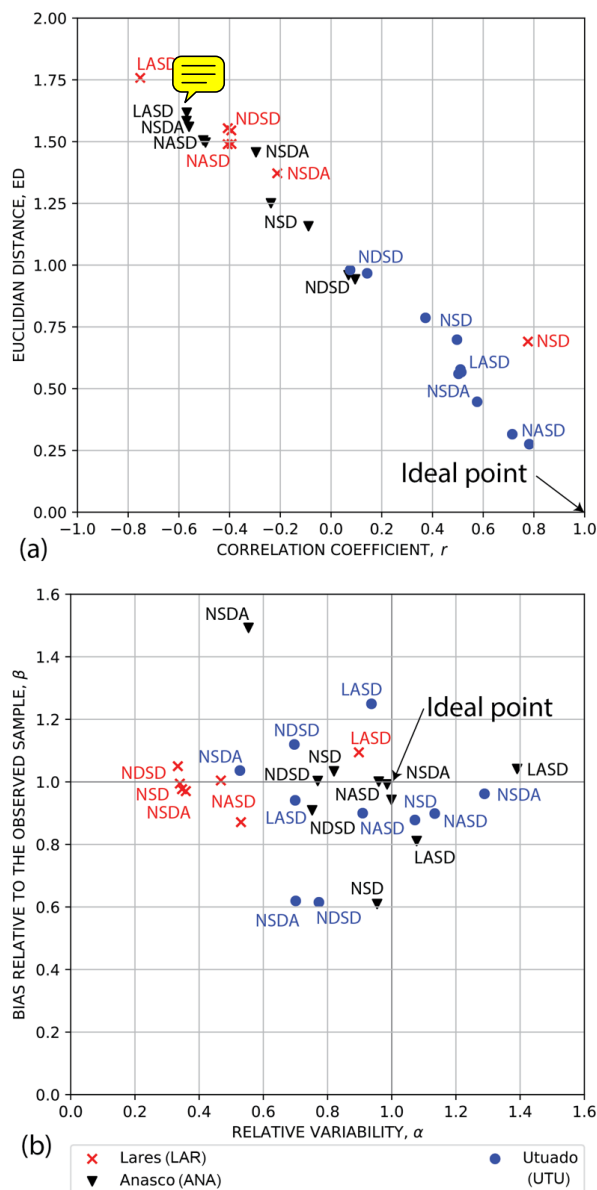
544 **4 Results**

545 **4.1 Soil-depth calibration**

546 We calibrated soil depth to field measurements (Fig. 6, step A.1) for three (ANA, LAR, UTU) of the four calibration
547 areas and calculated Euclidian distance from the ideal point, ED (Eq. 5), correlation coefficient, r (and other statistical
548 parameters as outlined in Tello 2020) to determine which models and parameter sets gave the closest match to field
549 observations (Fig. 8a, b). No soil depth calibration was performed for NAR as depth measurements in Naranjito were
550 mainly outside the area mapped by Bessette-Kirton et al. (2019c). Limiting the observed depths to landslide scars on
551 relatively unmodified slopes resulted in sample sizes of only seven or eight observation points (landslide sources) per
552 calibration area. Most soil-depth models for the Utuado calibration area (UTU) had acceptable performance as
553 indicated by positive correlation between observed and simulated depths (0.08 $\leq r \leq$ 0.78), and ED ranging from 0.28



554 to 0.99 (Fig. 8a; Tello 2020). Of these, the modified nonlinear area and slope (NASD) model had the smallest ED,
555 0.28, and the largest r , 0.78 (Fig. 8a). Other better-performing models were a nonlinear slope-dependent model with
556 linear area dependence (NSDA) and a linear area- and slope-dependent model (LASD) based on the wetness index
557 (Ho et al. 2012). In contrast, most soil-depth models for the Añasco (ANA) and Lares (LAR) calibration areas
558 performed poorly, with negative or small positive correlation ($r < 0.16$) and $0.69 < ED < 1.8$ (Fig. 8a). At LAR, only
559 the nonlinear slope dependent model (NSD, see Pelletier and Rasmussen 2009) had acceptable performance with $r =$
560 0.78 and $ED=0.69$ (Fig. 8a). The NASD model had α and β closest to 1, for both ANA and LAR (Fig. 8b).



561

562

563 Figure 8. Soil-depth model calibration measures for Anasco (ANA), Lares (LAR) and Utuado (UTU) calibration areas (Fig.

564 1). Performance is based on comparing maximum landslide depth at field-mapped landslide points against modeled depths

565 within a 5-m radius of the point. GPS point locations were corrected as needed by moving them to the centers of

566 corresponding landslide polygons mapped by Bessette-Kirton et al. (2019c). (a) Primary metrics, Euclidian distance from

567 the ideal point, ED (smaller is better), versus correlation coefficient, r , (b) bias relative to the observed sample, β , versus

568 relative variability, α . The ideal point is at $r=1$, $\alpha=1$, $\beta=1$. [Soil-depth models: LASD, linear area- and slope-dependent

569 model; NASD, nonlinear area- and slope-dependent model; NDS, nonlinear depth- and slope-dependent model; NSD,

nonlinear slope-dependent model; NSDA, nonlinear slope-dependent model with linear area dependence].



570 4.2 Soil model evaluation and slope-stability calibration results

571 Slope stability calibration compared F_1 values for previously determined ranges of c' and ϕ' (Fig. 5) for each of the
 572 soil depth models to find the best-performing combination of soil model and strength parameters for predicting
 573 landslide source locations in each calibration area (Fig. 6, steps A.3.a and A.3.b). For UTU, the NASD model
 574 performed best with the NSDA model close behind (Tello 2020) based on area under the TPR – FPR curve and
 575 distance of the curve from the ideal point. Parameter combinations and ROC results for the best-performing model in
 576 each area appear in Table 1. Despite poor soil depth model performance metrics for ANA and LAR (Fig. 8), the F_1
 577 calculations for the three calibration areas indicated that the NASD soil depth model had the greatest predictive
 578 strength for locations of landslide source areas in ANA, LAR, and UTU with similar results (Table 1). Despite lack
 579 of soil-depth calibration in NAR, results in this study area were like the other three calibration areas (Table 1). Values
 580 of δ_c near 60° gave the best soil-depth model results (Table 1), despite variability in the steepest slopes where
 581 landslides occurred in the different terranes (Fig. 3d, 4).

582
 583 **Table 1. Calibration results for 1D factor of safety, F_1 , with soil depth models by calibration area (Fig. 1). Positives and**
 584 **negatives in the ROC analysis based on total pixels within and outside the estimated source areas of landslide polygons**
 585 **mapped by Bessette-Kirton et al. (2019c) and whether the pixels have $F_1 > 1$ or $F_1 < 1$ (Tello 2020). [Symbols and**
 586 **abbreviations: NASD, non-linear area and slope dependent soil-depth model of Pelletier and Rasmussen (2009) as modified**
 587 **by Baum et al. (2021); H_{max} , maximum soil depth; δ_c , critical slope angle; R_d , diffusivity ratio; c' , soil cohesion for effective**
 588 **stress; ϕ' , angle of internal friction for effective stress; AUC, area under the curve of true-positive-rate (TPR) and false**
 589 **positive rate (FPR) (larger is better); d_{IP} , distance from the ideal point, (0,1), to nearest point on the TPR-FPR curve (smaller**
 590 **is better); Best F_1 , 1D factor of safety at point on the TPR-FPR curve nearest to the ideal point, (0,1), and therefore the**
 591 **most accurate F_1 classifier of landslide versus non-landslide grid cells for the particular model (closer to one is better); $^\circ$,**
 592 **degrees.]**

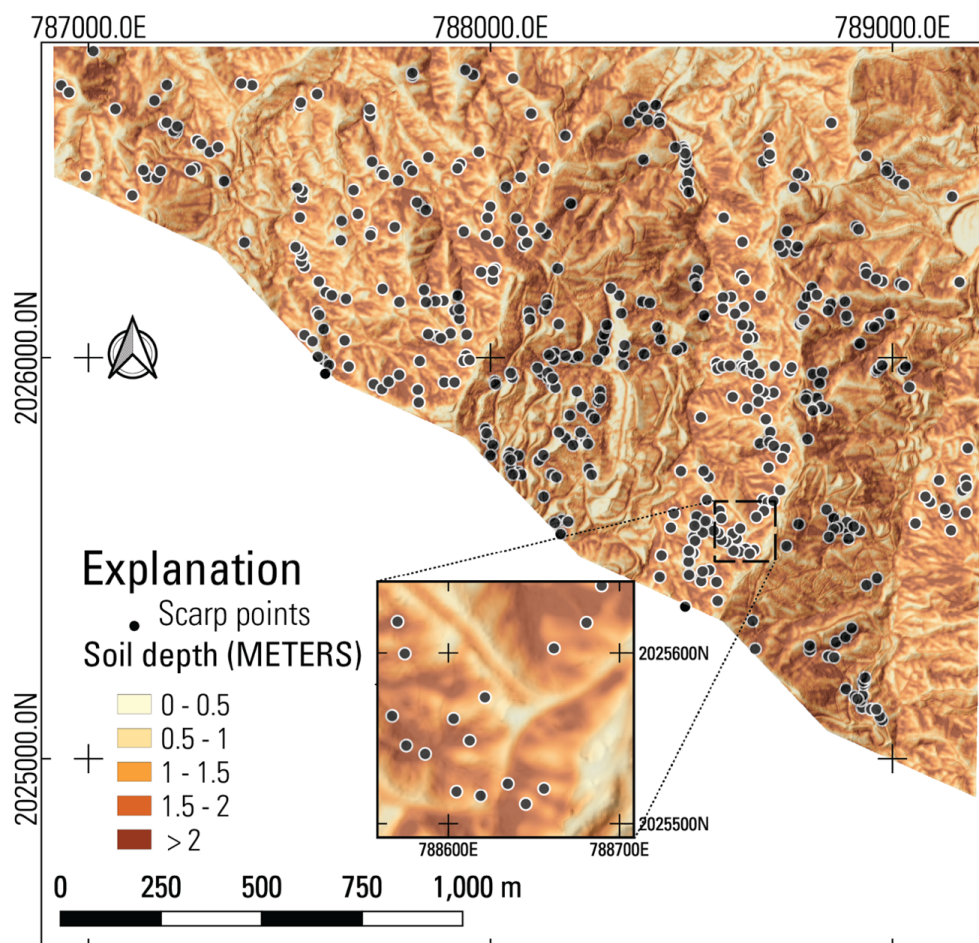
Calibration area	Soil Model	H_{max} (m)	δ_c ($^\circ$)	R_d	c' (kPa)	ϕ' ($^\circ$)	AUC	d_{IP}	Best F_1
Utuaado (UTU)	NASD	2.0	60	1.0	2.5	45°	0.67	0.48	1.5
Añasco (ANA)	NASD	3.0	60	0.16	4.5	45°	0.70	0.46	1.1
Lares (LAR)	NASD	3.0	60	0.25	4.5	45°	0.66	0.52	1.1
Naranjito (NAR)	NASD	3.0	60	0.2	4.0	45°	0.65	0.54	1.2

594 4.3 Modeled soil depth

595 Having completed the soil-depth model calibration (Sec. 4.1) and testing (Sec. 4.2), we modeled soil depth in the
 596 larger map tiles preparatory to analyzing slope stability (Fig. 6, step B.1). Each tile covers hundreds of km^2 , so we
 597 illustrate results using the NAR area, chosen to demonstrate that our susceptibility workflow can achieve very good
 598 results even with limited landslide source depths observations. As noted previously, insufficient field-measured
 599 landslide points prevented soil-depth model calibration (Sec. 4.1), but not model evaluation and slope stability



600 calibration (Sec. 4.2) for NAR. Figure 9 shows predicted soil depth for the best performing soil-depth model (based
601 on the slope-stability evaluations, Sec. 4.2) in NAR (see Fig. 1 for location). The model shown in Fig. 9 predicts
602 greater soil depth in hollows than on ridges. Other models that were tested (not shown) produced somewhat similar
603 results. Differences in model structure produce different responses to topographic features, including flat areas, road
604 cuts, and steep slopes. For example, the modified NASD and NSDA models predicted deep soils (≤ 3 m for parameters
605 chosen) in convergent areas, on steep slopes, including road cuts and embankments; thin soils on ridge crests, and thin
606 or no soil on downslope flat areas (see large flat area on east edge of Fig. 9). In contrast, the LASD and NDS models
607 predicted deep soils (≤ 3 m for parameters chosen) in convergent areas and on flats and thin soils on ridge crests and
608 steep slopes (except where they occur in strongly convergent topography). Features were more distinct in the three
609 nonlinear models, NASD, NSDA, and NDS, than in the linear LASD model.

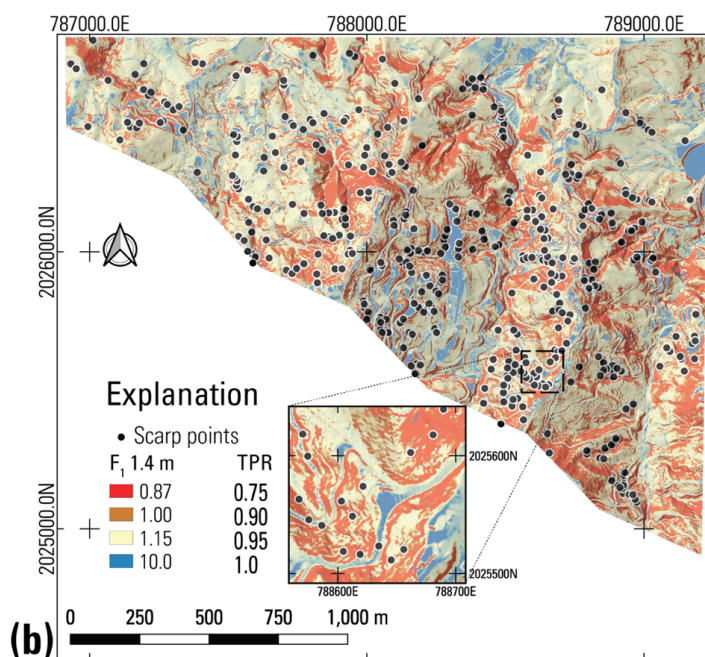
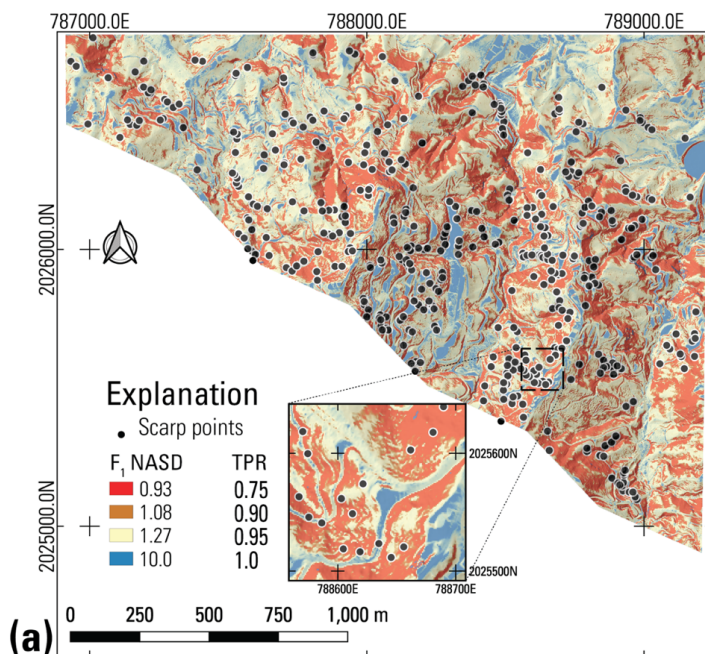


610
611 **Figure 9.** Best-performing version of soil depth maps from soil-depth models tested for the Naranjito (NAR) calibration
612 area in volcaniclastic terrane (Fig. 1). Topographic base derived from lidar by U.S. Geological Survey (2018), scarp points
613 from Besette-Kirton et al. (2019c). The modified Nonlinear Area- and Slope-dependent (NASD) model (modified from
614 Pelletier and Rasmussen 2009, as implemented by Baum et al. 2021) depicted here, was the overall best-fitting soil-depth
615 model for this terrane. Inset shows details of a 150 m by 150 m area, with thicker soil accumulation in concave areas.



616 **4.4 One-dimensional factor of safety**

617 Figure 10 shows F_1 optimized for NAR and calculated using TRIGRS and the soil model results in Fig. 9, as well as
618 F_1 for constant soil depth. Slopes steeper than 60° , the estimated critical slope angle, were treated as barren and stable
619 because landslides were very rare on slopes steeper than 60° (Fig. 3d). Soil strength parameters are within the ranges
620 obtained by sensitivity analysis of F_1 parameters ϕ' and c' over observed ranges of slope and depth of landslides
621 characterized in the field at ANA, LAR, UTU, and NAR (Fig. 5). The only landslide source locations available
622 throughout the three municipalities are the scarp points of Hughes et al. (2019). Due to location uncertainty, we used
623 a 3-m radius around the scarp points for defining true positives. Color thresholds on the maps (Fig. 10) are based on
624 F_1 at TPR of 0.75, 0.90, and 0.95. Consequently, thresholds for F_1 differ for each panel in Fig. 10. The same TPR
625 values (0.75, 0.90, 0.95) were used for picking F_3 thresholds for landslide initiation susceptibility across the entire
626 study area covering Naranjito, Utuado, and Lares Municipalities in the final maps (Supplemental Figures S1 and S2).



627
 628
 629
 630
 631
 632

Figure 10. Maps of Naranjito (NAR) calibration area in volcaniclastic terrane (Fig. 1) showing 1D factor of safety (F_1) results for a) soil-depth model shown in Figure 9 as well as b) constant average soil depth. Topographic base derived from lidar by U.S. Geological Survey (2018), scarp points from Bessette-Kirton et al. (2019c). True positives determined by minimum F_1 within a 3-m radius of the scarp points. (a) F_1 for NASD, the modified nonlinear area- and slope-dependent soil-depth model depicted in Fig. 9, (b) F_1 for constant soil depth of 1.4 m. Inset shows details of a 150 m by 150 m area.



633 Areas of low F_1 are similar in overall pattern between the two maps shown in Fig. 10 but differ in detail. These details
 634 include small areas of low F_1 unique to each model as well as variation in the extent of major areas of low F_1 . Many
 635 boundaries of the areas of low F_1 are ragged and small patches of yellow, indicating higher F_1 , occur within the larger
 636 red and orange areas of low F_1 . Differences in F_1 between the maps are attributable mainly to variation in soil depth
 637 and partly to variation in c' . The optimum value of c' varied depending on the characteristics of each soil model (Table
 638 2). The results shown in Fig. 10 are for the best-performing combination of c' and ϕ' for the soil-depth model at NAR
 639 (Fig. 9 and Sec. 4.2) and for constant average depth of 1.4 m.

640 The different F_1 patterns shown in Fig. 10 correspond to slightly different levels of predictive success. The AUC and
 641 distance from the ideal point (0,1) to the nearest point on the TPR-FPR curve, d_{IP} indicate that F_1 for constant depth
 642 has the highest predictive skill (AUC=0.88, d_{IP} =0.26, F_1 value nearest the ideal point, F_1 =0.9). Next, F_1 for the NASD
 643 model performed almost as well (AUC=0.86, d_{IP} =0.30, F_1 value nearest the ideal point, F_1 =1.0). When applied to the
 644 entire DEM tile covering Naranjito municipality, F_1 for constant depth and NASD tied with AUC = 0.86 and d_{IP} =
 645 0.30 (constant depth) and d_{IP} = 0.29 (NASD). Thus, the performance edge of constant depth is localized at NAR and
 646 does not extend across the entire Naranjito DEM tile. Other soil-depth models performed slightly worse (Table 2)
 647 consistent with results obtained by Tello (2020) for UTU. The slightly higher performance for F_1 with constant depth
 648 at NAR comes at the cost of the area classified as very high, high, or moderate susceptibility (TPR = 0.95) being more
 649 diffuse, with more ragged boundaries, than for F_1 with NASD (Fig. 10a, b). Varying the amount of cohesion used with
 650 a particular soil model caused small changes in the AUC, d_{IP} , and best F_1 as shown by the two entries for NDSD in
 651 Table 2.

652 **Table 2. Key inputs and performance measures for factor of safety calculations based on the infinite slope model (F_1), as**
 653 **implemented by TRIGRS, in the Naranjito calibration area (NAR). Performance is based on minimum F_1 within a 3-m**
 654 **radius of landslide scarp points mapped by Hughes et al. (2019). [Symbols and abbreviations: NASD, non-linear area and**
 655 **slope dependent soil-depth model of Pelletier and Rasmussen (2009) as modified by Baum et al. (2021); NSDA, non-linear**
 656 **slope dependent model of Pelletier and Rasmussen (2009) modified by Baum et al. (2021) to include linear area dependence;**
 657 **NDSD, non-linear slope and depth dependent model of Pelletier and Rasmussen (2009); LASD, linear area and slope**
 658 **dependent model of Ho et al. (2012); H_{max} , maximum soil depth; δ_c , critical slope angle; R_d , diffusivity ratio; C_0 , empirical**
 659 **constant used in LASD; c' , soil cohesion for effective stress; ϕ' , angle of internal friction for effective stress; AUC, area**
 660 **under the curve of true-positive-rate (TPR) and false positive rate (FPR) (higher is better); d_{IP} , distance from the ideal**
 661 **point, (0,1), to nearest point on the TPR-FPR curve (smaller is better); Best F_1 , 1D factor of safety at point nearest to the**
 662 **ideal point, (0,1), and therefore the most accurate F_1 classifier of landslide versus non-landslide grid cells for the particular**
 663 **model (closer to 1.0 is better); °, degrees ; -- not applicable.]**

Soil Model	H_{max} (m)	δ_c (°)	R_d or C_0	c' (kPa)	ϕ' (°)	AUC	d_{IP}	Best F_1	TPR at d_{IP}
NASD	3.0	60	0.20	4.0	45°	0.86	0.30	1.0	0.82
LASD	3.0	60	0.45	3.5	45°	0.85	0.31	1.1	0.84
NDSD	3.0	60	0.10	4.5	45°	0.82	0.36	1.2	0.75
NDSD	3.0	60	0.10	2.5	45°	0.86	0.32	1.0	0.89
NSDA	3.0	60	0.10	4.5	45°	0.85	0.30	1.1	0.80
Constant	1.4	60	--	4.0	45°	0.88	0.26	0.9	0.79

664



665 **4.5 Quasi-three-dimensional factor of safety**

666 Figure 11 shows F_3 computed using the soil-depth model in Fig. 9 and constant soil depth of 1.4 m. Predictive skill
 667 for F_3 is somewhat less than F_1 ; AUC is 0.05 – 0.08 less for F_3 than corresponding F_1 (Tables 2 and 3). The only
 668 exception is for the constant soil depth model results where F_3 has the highest AUC, 0.94, of all cases tested (Fig. 12a
 669 and 12b). Despite the overall slightly worse performance of F_3 it provided smoother boundaries on the landslide
 670 susceptible areas (Fig. 11a, b), which also are more continuous than corresponding F_1 landslide susceptible areas (Fig.
 671 10). The lower AUC values resulted from the F_3 susceptible areas covering slightly more land area than the
 672 corresponding F_1 areas at the same TPR. Therefore, the F_3 susceptibility maps are more conservative than their F_1
 673 counterparts.

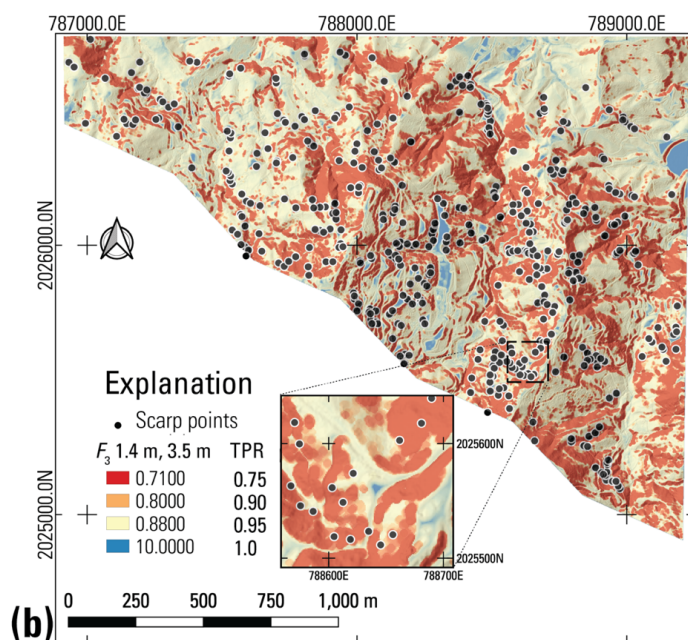
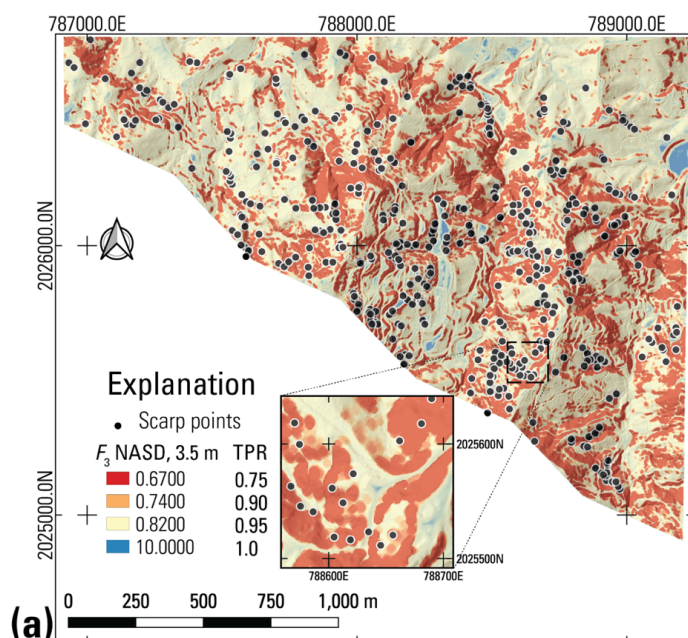
674 **Table 3. Key inputs and performance measures for factor of safety calculations based on a quasi-3D limit-equilibrium slope**
 675 **stability model (F_3) in the Naranjito calibration area (NAR). Performance is based on minimum F_3 within a 3-m radius of**
 676 **landslide scarp points mapped by Hughes et al. (2019). [Symbols and abbreviations: NASD, non-linear area and slope**
 677 **dependent soil-depth model of Pelletier and Rasmussen (2009) as modified by Baum et al. (2021); NSDA, non-linear slope**
 678 **dependent model of Pelletier and Rasmussen (2009) modified by Baum et al. (2021) to include linear area dependence;**
 679 **NDS, non-linear slope and depth dependent model of Pelletier and Rasmussen (2009); LASD, linear area and slope**
 680 **dependent model of Ho et al. (2012); H_{max} , maximum soil depth; δ_c , critical slope angle; R_d , diffusivity ratio; C_0 , empirical**
 681 **constant used in LASD; c' , soil cohesion for effective stress; ϕ' , angle of internal friction for effective stress; AUC, area**
 682 **under the curve of true-positive-rate (TPR) and false positive rate (FPR); d_{IP} , distance from the ideal point, (0,1), to nearest**
 683 **point on the TPR-FPR curve; Best F_3 , 3D factor of safety at point nearest to the ideal point, (0,1), and therefore the most**
 684 **accurate F_1 classifier of landslide versus non-landslide grid cells for the particular model (closer to 1.0 is better); °, degrees.]**

Soil Model	H_{max} (m)	δ_c (°)	R_d or C_0	c' (kPa)	ϕ' (°)	Trial surface radius (m)	AUC	d_{IP}	Best F_3	TPR at d_{IP}
NASD	3.0	60	0.20	0.5	45°	3.5	0.80	0.38	0.9	0.86
NASD	3.0	60	0.20	0.5	45°	6.5	0.75	0.45	0.9	0.66
NASD	3.0	60	0.20	0.5	45°	9.5	0.71	0.50	1.0	0.86
LASD	3.0	60	0.45	0.5	45°	3.5	0.78	0.44	1.0	0.89
NDS	3.0	60	0.10	0.5	45°	3.5	0.78	0.40	0.9	0.71
NSDA	3.0	60	0.10	0.5	45°	3.5	0.80	0.37	0.9	0.78
Constant	1.4	60	--	0.5	45°	3.5	0.92	0.23	1.0	0.94

685
 686 Tests indicated that trial surfaces having a map-view radius of 3.5 m provided more accurate estimates of susceptible
 687 areas than larger trial surfaces (6.5-m and 9.5-m radius). Other things being equal, larger trial surfaces resulted in
 688 smaller AUC and larger d_{IP} (Table 3, Fig. 12b). The larger trial surfaces tended to widen the susceptible areas and
 689 smooth their boundaries, with the result that a larger percentage of the calibration area was classified as susceptible
 690 (9.5-m radius, 85%; 6.5-m radius, 83%; 3-m radius, 78% for examples in Table 3). In addition, the 3.5-m radius
 691 produced a trial surface close in size (7.5 – 7.9 m wide, with an area of 46 – 48 m² at the ground surface for 1-m depth
 692 on 30° – 40° slopes) to the median horizontal areas of landslide sources mapped in NAR, 51 m², in UTU2, 42 m², and
 693 in LAR2 64 m² (Fig. 3c).



694



695

696

697

698

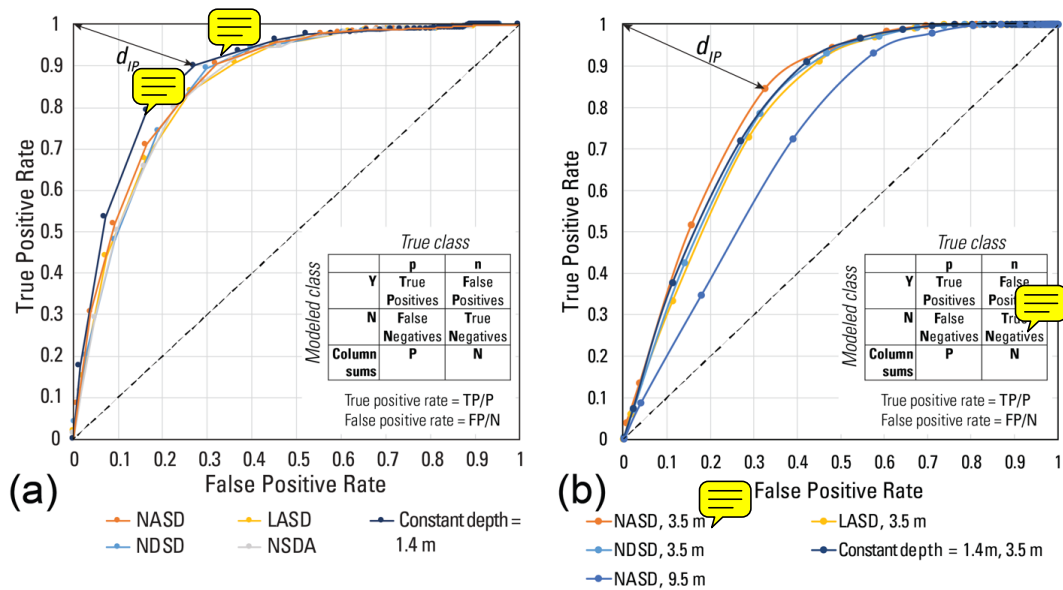
699

700

Figure 11. Maps of Naranjito (NAR) calibration area in volcaniclastic terrane (Fig. 1) showing quasi-3D factor of safety, F_3 , results for the soil depth models shown in Figure 9. (a) F_3 for the modified nonlinear area and slope dependent (NASD) soil-depth model depicted in Fig. 9, (b) F_3 for constant soil depth of 1.4 m. Inset shows details of a 150 m by 150 m area. The calculation of F_3 used a trial surface of 3.5-m map-view radius (Fig. 7). Topographic base derived from lidar by U.S. Geological Survey (2018), scarp points from Bessette-Kirton et al. (2019c).



701



702

703 **Figure 12.** Graphs of true positive rate (TPR) versus false positive rate (FPR) for factor of safety maps in Naranjito
 704 calibration area (NAR in Fig. 1a, 1c). Inset shows confusion matrix and formulas defining true positive rate and false
 705 positive rate. Double-headed arrow indicates distance from ideal point (d_{IP}) for the results of the factor of safety with
 706 the smallest d_{IP} . (a) TPR-FPR results for 1D factor of safety (F_1) in Fig. 10, as well as results for F_1 using other soil-depth models
 707 that were tested during the calibration process. (b) TPR-FPR results for quasi-3D factor of safety (F_3) in Fig. 11, as well as
 708 results for F_3 using other soil depth models and one with a larger (NASD, 9.5-m radius) trial surface. [Soil-depth models:
 709 LASD, linear area- and slope-dependent model (Ho et al. 2012); NASD, modified nonlinear area- and slope-dependent
 710 model (modified from Pelletier and Rasmussen 2009); NDS, nonlinear depth- and slope-dependent model (Pelletier and
 711 Rasmussen 2009); NSD, nonlinear slope-dependent model (Pelletier and Rasmussen 2009); NSDA, nonlinear slope-
 712 dependent model with linear area dependence (modified by Baum et al. 2021 from NSD model of Pelletier and Rasmussen
 713 2009)].

714 4.6 Susceptibility categories and predictive strength

715 Computing F_3 over the combined study areas of Lares, Utuado, and Naranjito municipalities produced somewhat
 716 different results than in the calibration areas. Calibration areas have very high landslide densities, with average density
 717 of 182 scarps/km² at NAR. However, landslide density varies considerably across each municipality. Based on positive
 718 correlation between low F_3 and landslide scarp points mapped by Hughes et al. (2019), we established susceptibility
 719 categories based on percentages of landslides enclosed by successive susceptibility categories as noted previously and
 720 as shown in Table 4. Increasing density of observed landslides is consistent with increasing susceptibility. Very high
 721 susceptibility (typically > 118 scarp points/km²) characterizes 23% of the total study area and 21%, 43%, and 45% of
 722 the area underlain by marine volcanoclastic, submarine basalt, and granitoid rocks, respectively. Almost all karst areas
 723 underlain by limey sediments had low susceptibility (< 2 scarp points/km²) (Baxstrom et al. 2021b). Based on the
 724 information in Table 4, the AUC for the entire map area is 0.84, and d_{IP} is 0.34.

725 Due to physical (subsurface conditions, ground-failure mechanisms) and conceptual (parameters, models)
 726 uncertainties, the F_3 value at the boundary between high and moderate susceptibility is slightly less than 1 (0.97, Table



727 4). Although the strength parameters could be increased to achieve $F_3 = 1.0$ at TPR = 0.90, we also wanted to keep F_3
 728 at TPR = 0.95 relatively low while keeping $F_3 > 1$ under dry conditions for as much area as possible. Our final model
 729 parameters represent a compromise between stable slopes ($F_3 > 1$) under dry conditions and low factor of safety (F_3
 730 < 1) for highly susceptible slopes under presumed wettest conditions.

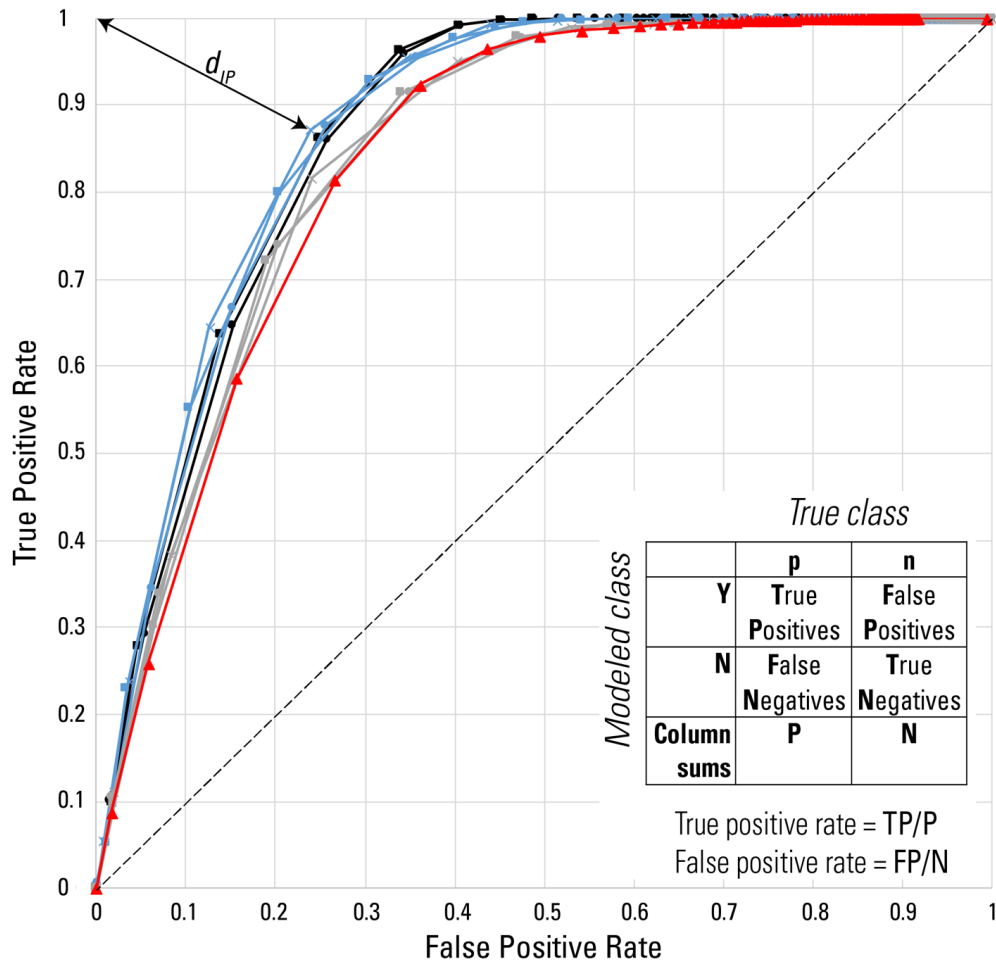
731 Recent, detailed mapping of source areas provided an opportunity to further test performance of the pre-Hurricane
 732 María F_3 map (output from step B.5, Fig. 6). Figure 13 shows TPR-FPR curves for the pre-Hurricane María F_3 map
 733 tested against Hurricane María landslide source polygons (Baxstrom et al. 2021a; Einbund et al. 2021a, 2021b) and
 734 against scarp points (Table 4). The AUC range, 0.85 – 0.88, is somewhat greater than obtained by testing within a 3-
 735 m radius of the scarp points, 0.84.

736

737 **Table 4. Landslide susceptibility categories based on minimum value of quasi-3D factor of safety, F_3 , within a 3-m radius**
 738 **of landslide scarp points mapped by Hughes et al. (2019) for all three municipalities. For consistency, F_3 thresholds below**
 739 **are based on F_3 calculated using pre-Hurricane María lidar topography and scarp locations of landslides induced by**
 740 **Hurricane María.**

Landslide Susceptibility	F_3 threshold	Landslide scarp points enclosed (percent)	Landslide scarp points enclosed within increment (number)	Area within increment (km ²)	Landslide points within increment (percent)	Incremental Landslide density (scarps/km ²)
Very High	≤ 0.87	75	27370	232	75	118
High	≤ 0.97	90	5474	108	15	51
Moderate	≤ 1.05	95	1825	68	5	27
Low	> 1.05	100	1824	610	5	3
Total	$0 < F_3 \leq 10$	100	36493	1018	100	36

741



- NASD, Utuado ($N_p=1442$, AUC=0.87)
- 1.4 m, Utuado ($N_p=1442$, AUC=0.87)
- NASD, Naranjito ($N_p=440$, AUC=0.87)
- 1.4 m, Naranjito ($N_p=440$, AUC=0.88)
- ×— NDSO, Naranjito ($N_p=440$, AUC=0.88)
- NASD, Lares ($N_p=1442$, AUC=0.85)
- NASD, Lares ($N_p=1442$, AUC=0.85)
- ×— NDSO, Lares ($N_p=1442$, AUC=0.85)
- ▲— NASD, Composite map area ($N_{sc}=36494$, AUC=0.84)

742

743 **Figure 13.** Graph of true positive rate versus false positive rate for pre-Hurricane María susceptibility models across the
 744 study area tiles tested against head-scarp points (Hughes et al. 2019) and source polygons for Lares (Einbund et al. 2021b),
 745 Naranjito (Baxstrom et al. 2021a), and Utuado (Einbund et al. 2021a) with confusion matrix and formulas defining true
 746 positive rate (TPR) and false positive rate (FPR). Double-headed arrow indicates distance from ideal point (d_{IP}) for
 747 Naranjito source polygons and F_3 computed using NDSO soil depth. True positive rates are based on minimum value of the
 748 quasi-3D factor of safety, F_3 , within the mapped source polygons or within a 3-m radius of the scarp points. Results for
 749 scarp points cover the final pre-Hurricane María susceptibility maps of Lares, Utuado, and Naranjito municipalities.
 750 Results for the landslide source polygons cover parts of the component tiles (Fig. 1). Landslide source mapping for Lares
 751 and Utuado (Einbund et al. 2021a, b) are near LAR and UTU (LAR2, UTU2, Fig. 1b). The graph compares F_3 performance
 752 based on the modified nonlinear area- and slope-dependent (NASD, modified from Pelletier and Rasmussen 2009) soil-
 753 depth model and two alternates: constant depth of 1.4 m, and the nonlinear depth- and slope-dependent soil-depth model
 754 (NDSO, Pelletier and Rasmussen 2009), with strength parameters and other inputs held constant. AUC denotes area under
 755 the curve of TPR versus FPR, N_p is the number of landslide source polygons, and N_{sc} is the number of scarp points.



756 5 Discussion

757 Our analyses presented in the previous section (Sect. 4.6) indicate that the landslide susceptibility assessment
758 successfully identifies areas where high percentages of Hurricane María landslides occurred. In succeeding
759 paragraphs, we discuss some of the strengths, limitations, and unexpected findings of our approach and results.

760 Optimum ranges of internal friction angles for all three terranes (Fig. 5) are higher than commonly reported, but
761 consistent with measured values of ϕ' for low normal stress (Likos et al. 2010). Most reported values of ϕ' for soils
762 like those in the study area range from 17° to 41° as noted previously (Sec. 3.2) and are usually based on tests at
763 normal stress greater than 100 kPa. In contrast, samples collected at two field monitoring sites tested at low and
764 moderate normal stresses (Smith et al. 2020) using equipment and procedures described by Likos et al. (2010) had
765 high friction angles for low normal stress. Smith et al. (2020) reported $\phi' = 34.8^\circ - 35.5^\circ$ ($c' = 0 - 4.4$ kPa) for two
766 samples tested at effective normal stress, σ'_n , less than 120 kPa, $\phi' = 45.6^\circ$ for a sample tested at $\sigma'_n \leq 30$ kPa, and ϕ'
767 $= 53.9^\circ$ for another sample tested at $\sigma'_n \leq 7$ kPa. Significantly, shear stress was considerably higher than normal stress
768 for nearly all individual tests at $\sigma'_n \leq 15$ kPa, and many at $\sigma'_n \leq 30$, consistent with $\phi' > 45^\circ$ at low normal stress. In
769 addition to evidence for high internal friction angles at low normal stress, which is particularly relevant to abundant
770 thin (< 0.5 m) landslides in Utuado, three other factors could contribute to stability and reduce the magnitude of ϕ'
771 required to explain stability during dry conditions: (1) Soil suction measured at the sites between rainfall (Smith et al.
772 2020) indicates that suction stress probably contributes to stability. Preliminary tests indicate that considering modest
773 amounts of suction stress (less than a few tens of kilopascals) during dry conditions in the analysis depicted by Fig. 5
774 shifts the cells having high TPR toward lower ranges of ϕ' . For example, increasing initial suction stress by -1 kPa
775 shifts the optimum range of ϕ' to $35^\circ - 40^\circ$ for the submarine basalt and chert landslides compared to the $45^\circ - 50^\circ$
776 range in Fig. 5d. (2) Root resistance also likely contributes to slope stability to depths of about 0.5 – 0.6 m. Due to
777 high annual rainfall, vegetation in the study areas tends to be shallow-rooted so that significant root resistance would
778 decline rapidly below about 0.4 – 1.1 m depth (Simon et al. 1990; Larsen 2012). (3) Lateral stress variation also
779 contributes to slope stability. Even in quasi-3D limit-equilibrium as used in computing F_3 , combined resistance of
780 neighboring grid cells (columns) and toe wedge contributes to stability and reduces the values of ϕ' and (or) c' needed
781 to achieve stability of a potential landslide under dry conditions (Tables 2 and 3).

782 Our modelling workflow makes a few trade-offs to create a relatively conservative map of potential landslide sources
783 that accounts for uncertainties. These trade-offs are between speed and simplicity of the assessment, statistical
784 accuracy, and continuity of susceptibility zones. Some of the modelling steps (soil depth and F_3) add complexity,
785 increase time needed to model susceptibility, and slightly reduce performance metrics (AUC and d_{IP}) compared to F_1
786 with constant soil depth. In exchange, soil depth and F_3 create more continuous susceptibility zones, join neighboring
787 groups of high-susceptibility pixels, and eliminate isolated, commonly errant, pixels of high landslide susceptibility
788 (Fig. 10 and 11). The increased continuity of the susceptibility zones makes them easier to implement in land use and
789 emergency management. In addition, the potential source areas delineated on the map by the high and very high
790 susceptibility areas provide areas susceptible to shallow landslides for estimating potential landslide runoff and debris-
791 flow inundation (Brien et al. 2021). Much of the reduction in AUC for F_3 results from using the minimum factor of



792 safety value computed for any trial landslide that includes a grid cell. Consequently, very high and high susceptibility
793 zones for F_3 are broader than for F_1 and thereby have a buffer along their edges. Nevertheless, as indicated by various
794 performance metrics and landslide densities in the susceptibility classes, the landslide assessment successfully
795 distinguishes areas having different levels of susceptibility to landslide initiation (Tables 3, 4) despite these trade-offs.
796 Although F_1 for constant depth has slightly better performance metrics (the highest AUC and smallest d_{IP}) than F_1 for
797 any of the soil depth models calibrated to landslide source depths (Table 2, Fig. 12a) at NAR, its performance metrics
798 are comparable to the nonlinear soil-depth models elsewhere. Our field observations indicate that depth of shallow,
799 rainfall-induced landslides is well correlated to depth of mobile regolith ("soil") due to strength and permeability
800 contrasts at its base. Soil-depth models represent the distribution of soil depth more consistently with field conditions
801 than constant depth in many settings (Pelletier and Rasmussen 2009; Ho et al. 2012; Catani et al. 2010; Nicótiña et al.
802 2011; Gomes et al. 2016; Patton et al. 2018). Performance metrics ($ED = \sqrt{2}$; mean-squared error, $MSE = \sigma_o^2$) indicate
803 average depth was a poorer predictor of observed landslide depth than any of the models Tello (2020) tested for
804 Utuado. Despite odd differences in how the models estimate soil depth on mid-slope benches and flat valley bottoms,
805 the models we tested (NASD, NSDA, NDS, LASD) predict thinner soils on ridge crests and thicker soils in hillside
806 hollows, consistent with patterns observed in Puerto Rico and elsewhere for dissected topography (Roering 2008). For
807 example, mean depths of landslide sources from field mapping in Puerto Rico were 3.25 m (for concave slopes), 2.5
808 m (for convex slopes), 2.7 m (for planar slopes; Schulz et al. 2023). The unexpected, good performance of F_1 for
809 constant soil depth at NAR points out limitations of soil depth models and may result in part from widespread
810 modifications to the landscape resulting from agriculture, road (e.g., Ramos-Scharrón et al. 2021) and building
811 construction, and other activities. Effects of these activities may have influenced the locations of shallow landslides
812 sufficiently to weaken correlation between landslide location and topographic features that influence soil depth (as at
813 LAR and ANA, Fig. 8a). The high degree of slope modification (roads and terraces) in the NAR calibration area is
814 likely a determining factor in F_1 performance there (Fig. 10). Identifying specific areas or features where constant-
815 depth F_1 classifies susceptibility differently than F_1 with other soil-depth models might reveal potential improvements.
816 Computing F_1 using the modified NASD soil-depth model resulted in the areas assigned to the moderate, high, and
817 very high susceptibility classes being more clearly delineated with little or no loss of performance compared to using
818 constant depth. The susceptibility zones in the constant-depth F_1 susceptibility map (Fig. 10b) are more diffuse or
819 fragmented (less continuous) than for the NASD soil depth (Fig. 10a) and other soil models we tested. Fragmentation
820 also occurred for susceptibility zones defined by slope categories (Fig. S3a). As noted previously, this improved
821 delineation came with only a slight reduction in AUC (0.88 to 0.86) and small increase in d_{IP} (0.26 to 0.30) for NAR.
822 When applied to the entire DEM tile covering Naranjito municipality, performance of F_1 for constant depth and F_1 for
823 NASD tied with each other and with slope categories (AUC = 0.87, d_{IP} = 0.29 - 0.30). As noted previously, when
824 checked against detailed source mapping, the performance metrics for F_3 are better than when compared against the
825 scarp points (Fig. 13). In addition, differences in performance metrics between constant depth and the NDS model
826 and modified NASD model are negligible.

827 Other things being equal, the quasi-3D stability analysis, F_3 , has a somewhat smaller AUC and larger d_{IP} , compared
828 to F_1 (Tables 2 and 3), but improves the final map. The improvements are better separation between the different



829 susceptibility classes (Fig. 10 and 11) and a slightly more conservative map compared to F_1 , which is helpful for life-
830 safety based land use planning and emergency response scenarios. With $AUC=0.80$ and $d_{IP}=0.38$ for F_3 based on the
831 modified NASD soil-depth and 3.5 m radius for the trial surface (Table 3), F_3 successfully identifies potential landslide
832 sources at NAR. For the entire map area, the AUC (0.84) and d_{IP} (0.33) scores are slightly better (Table 4, Fig. 13),
833 due in part to the large area of low landslide susceptibility that is underlain by limey sediments and characterized by
834 cone karst. By considering slope stability at the scale of representative landslide sources (median area, Fig. 3c), F_3
835 eliminates isolated grid cells and tiny clusters of 2 – 4 cells that likely are classified incorrectly by F_1 as highly or very
836 highly susceptible due to locally steep slopes at the pixel scale (1 m). Such isolated cells and clusters could be
837 eliminated after analysis, but boundaries of susceptible areas would remain somewhat ragged. In contrast our approach
838 provides an objective method for eliminating the isolated pixels and smoothing the boundaries. F_3 bridges gaps
839 between neighboring areas of low F_1 and thereby maps susceptible areas that are more continuous and with smoother,
840 more definite boundaries than F_1 . Thus, F_3 further improves delineation of susceptible areas beyond improvements
841 achieved by using the modified NASD soil-depth model with F_1 . **Maps having continuous, clearly delineated areas**
842 **assigned to each susceptibility class such as those obtained by using F_3 reduce guesswork in making land use and**
843 **emergency management decisions by eliminating the ragged, transitional boundaries obtained with F_1 .** For example,
844 to compare the insets in Figs. 10 and 11 to each other as well as slope categories (Fig. S3a) and F_3 based on the NDS
845 soil-depth model (Fig. S3d), see Fig. S3b, c, e and f. Well-defined potential landslide source areas also allow
846 estimation of areas susceptible to potential downslope runout and downstream inundation (Brien et al. 2021).
847 Performance metrics for F_3 considering detailed source mapping (Fig. 13) are sufficiently high ($0.85 \leq AUC \leq 0.88$)
848 to consider F_3 a very successful indicator of landslide susceptibility in our study area. As the basis for our final
849 susceptibility maps, we selected the F_3 map derived from the modified NASD soil depth model (Fig. 11a) because of
850 its high AUC combined with its well-defined source areas and the realistic modeled soil depths for estimating potential
851 landslide volumes. Model input parameters for the final maps are summarized in Supplemental Figures S1 and S2.
852 The susceptibility analysis portrayed in Fig. 11 and our final maps (Supplemental Figures S1 and S2) are valid
853 throughout the three municipalities despite the variable density of Hurricane María landslides throughout the map area
854 (Bessette-Kirton et al. 2017; Hughes et al. 2019) and within each susceptibility class. High landslide density generally
855 corresponds to low F_3 (Table 4); however, not all susceptible areas were equally affected by Hurricane María. Thus,
856 although some areas of low F_3 , particularly in Naranjito, had low landslide density, the low density does not invalidate
857 the susceptibility assessment of the potential for future landslides. Factors such as antecedent soil moisture are known
858 to have affected the density of landslides induced by Hurricane María (Bessette-Kirton et al. 2019a) and were
859 addressed in the statistically based island-wide landslide susceptibility assessment of Hughes and Schulz (2020a).
860 Notably Naranjito had much lower root-zone soil moisture immediately after the hurricane than Utuado and Lares
861 (Fig. 26 of Hughes and Schulz 2020a). Variable rainfall intensity and duration are also known to affect landslide
862 response of susceptible areas (Larsen and Simon 1993; Pando et al. 2005). Intensity and duration are known to have
863 varied during Hurricane María, causing further differences in landslide density. Our assessment considered fully
864 saturated conditions with the water table at the ground surface to depict likely wettest-case soil moisture effects,
865 including high antecedent soil wetness, as well as high intensity and long-duration rainfall. Thus, it was not necessary



866 to specifically model antecedent soil moisture conditions. Less-severe conditions may produce landslides in the same
867 general areas as predicted by our assessment, however, in lower numbers than observed following Hurricane María.
868 Setting the boundaries between susceptibility classes based on F_1 or F_3 corresponding to specific values of TPR rather
869 than setting boundaries based on theoretical values of F_1 or F_3 (such as $F_3 = 1.0$) reduces uncertainty and ensures
870 correspondence between landslide density and degree of landslide susceptibility. Soil, saprolite, and bedrock are
871 inherently heterogenous. Their hydraulic and strength properties (and corresponding parameters) vary spatially at all
872 scales (Terzaghi et al. 1996). Other studies have applied probabilistic approaches and sensitivity analyses have been
873 applied successfully to address parameter uncertainty and improve accuracy of physically based modelling of landslide
874 susceptibility (Raia et al. 2014; Zieher et al. 2017; Canli et al. 2018). Many parameter combinations (c' and ϕ') can
875 achieve similar levels of predictive accuracy in computing F_1 for observed distributions of landslide slope and depth
876 (Baum et al. 2019; Baum 2021). These and other uncertainties such as transient pore-water pressures, subsurface
877 features, heterogeneity, and other factors, weaken the link between theoretical values of F_1 or F_3 and estimated
878 likelihood of failure for site-specific cases when applying limit-equilibrium slope stability analysis over wide areas.
879 On the other hand, maps classified based on TPR have a strong link to susceptibility. Such maps are readily comparable
880 to each other when F_1 or F_3 values are computed with different parameters, as they show like outcomes (areas that
881 capture 75%, 90% and 95% of observed landslides in this study). Comparing like outcomes focuses on differences
882 and uncertainties that affect the quality of the susceptibility assessment that might be masked by comparing the maps
883 when classified using the same F_1 or F_3 values. In this study, low values of F_1 and F_3 correspond to high observed
884 Hurricane María landslide density (Table 4), as would be expected. The selected boundaries for susceptibility classes
885 ensure a meaningful distinction between average landslide density in the successive classes (Table 4).
886 The susceptibility map correctly predicts locations of most landslides that are deeper than 3 m, despite the maximum
887 modeled soil depth of 3 m more typical of shallow landslides. Ten of the landslides summarized in Fig. 3e are deeper
888 than 3 m. Most (nine) are within the Naranjito tile (Fig. 1), and the other is in Lares. The mapped point on each
889 landslide headscarp and adjoining or surrounding slope was within the high or very high susceptibility zone for seven
890 of the ten deep landslides. The other three had head scarps on a gently sloping area (road or pad) that was set back a
891 few meters from the steep slope, but the adjoining slope with the landslide body was within the high and very high
892 susceptibility zones. Although the predicted locations might be right for the wrong reason (predicting a shallow
893 translational landslide rather than a deeper, translational, or rotational landslide), it is nevertheless encouraging that
894 the locations of even the deep landslides are identified for the sake of hazard assessment and planning. This probably
895 occurred because the deep landslides occurred well within the same slope range as other mapped landslides (Fig. 3,
896 4).
897 Despite the simplicity of soil and water parameters, the maps successfully predicted the effects from Hurricane María.
898 Calibrating with field data from the small calibration areas (ANA, LAR, UTU, and NAR, Fig. 1) and then testing with
899 the island-wide scarp points (Hughes et al. 2019) confirmed the successes of our approach (Supplemental Figures S1
900 and S2). Testing with detailed landslide source maps (Baxstrom et al. 2021a; Einbund et al. 2021a, 2021b) strengthens
901 our results even though they cover only a fraction of the study area.



902 The workflow outlined in Fig. 6 can be simplified in areas where few data are available. An accurate digital elevation
903 model and accurate landslide inventory with measurements of source area size, depth, and slope (Fig. 3) are the most
904 critical data for a landslide susceptibility analysis. Strength parameter ranges can be estimated from landslide source
905 depth and slope (Fig. 4, 5). Soil model calibration can be bypassed by assuming constant average landslide source
906 depth. Strength parameters can then be refined using the procedure described in Sect. 3.5. Alternately a soil model
907 and strength parameters can be calibrated simultaneously to the inventory as we did for the NAR calibration area.
908 Calculation of pressure head, F_1 and F_3 can then proceed as outlined in Sect. 3.4.2, 3.4.3, 3.4.4, and 3.9, followed by
909 validation and evaluation (Sect. 3.11). Compared to a map based on the simplest of landslide susceptibility approach,
910 slope ranges with its ragged, fragmented susceptibility zones, our procedure creates cohesive landslide susceptibility
911 zones that have smooth, buffered boundaries with only a slightly lower AUC score (0.84) than for slope (0.87) across
912 the entire study area.

913 **6 Conclusions**

914 We defined a workflow for assessing landslide susceptibility using multiple modelling stages and successfully applied
915 it using high-resolution (1-m) topography over a large (about 1000 km²) geographic area in the central mountains of
916 Puerto Rico (Fig. 1). The workflow includes modelling soil depth, pressure head, and limit-equilibrium slope stability
917 (Fig. 6). Although calibration studies showed that assuming constant average soil depth as input for 1D (infinite-slope)
918 factor of safety against landsliding, F_1 , gave the best performance metrics in a 2.5 km² calibration area, use of a soil-
919 depth model more clearly delineated areas susceptible to landslide initiation with only a modest reduction in the AUC
920 from 0.88 to 0.86. Using a quasi-3D limit-equilibrium slope stability analysis, the factor of safety, F_3 , further refined
921 the susceptibility assessment by more clearly delineating boundaries between the different susceptibility classes and
922 by assessing stability at the scale of the observed median-sized landslides. Despite further reduction in AUC to 0.80
923 for the NAR calibration area, the map based on F_3 is more readily usable in certain applications than a map based on
924 F_1 , and it still performs well as a classifier of landslide susceptibility. Performance metrics for the F_3 map of the entire
925 ~1000 km² study area, $AUC = 0.84$ and $d_{IP} = 0.34$, are slightly better than results at the NAR calibration area.
926 Performance measured against detailed source mapping of selected areas is even better: $0.85 \leq AUC \leq 0.88$ and 0.27
927 $\leq d_{IP} \leq 0.33$. These metrics indicate the map is suitable for planning, regulation, and emergency preparedness decisions
928 at the municipality scale. The map may also be used to assess hazards, such as ground collapse, resulting from landslide
929 initiation. Source area delineation as shown on maps may also be used for defining landslide starting locations and
930 surface area needed to assess areas with potential downslope movement of sediment mobilized by future landslides.

931 **Code availability**

932 Computer codes used in this study are available from the U.S. Geological Survey software repository as follows:
933 TRIGRS 2.1, <https://doi.org/10.5066/F7M044QS>; REGOLITH, <https://doi.org/10.5066/P9U2RDWJ>; and Slabs3D,
934 <https://doi.org/10.5066/P9G4I8IU>.



935 **Data availability**

936 The pre-event (2015) and post-event (2018) lidar topographic data used in this study are available through the National
937 Map at <https://apps.nationalmap.gov/lidar-explorer/#/>. Soil mapping databases used to estimate soil properties are
938 available from the Natural Resources Conservation Service at [https://www.nrcs.usda.gov/resources/data-and-](https://www.nrcs.usda.gov/resources/data-and-reports/web-soil-survey)
939 [reports/web-soil-survey](https://www.nrcs.usda.gov/resources/data-and-reports/web-soil-survey). Other data are available from the U.S. Geological Survey ScienceBase digital repository as
940 follows: Summaries of geotechnical data, <https://doi.org/10.5066/P9UXTQ4B>; model input and output raster grids
941 and model parameter input files used to produce the large maps (Supplemental Figures S1 and S2),
942 <https://doi.org/10.5066/P9C1U0LP>; Landslide head scarp points, <https://doi.org/10.5066/P9BVMD74>; landslide
943 polygons, <https://doi.org/10.5066/F7JD4VRF>, <https://doi.org/10.5066/P9GBGA4I>,
944 <https://doi.org/10.5066/P9YYU7W1>, <https://doi.org/10.5066/P9EASZZ7>, and <https://doi.org/10.5066/P9ZNUR1P>.

945 **Author contribution**

946 RB, WS, MR and DB planned the study. WS managed the project. MT carried out model calibrations. RB developed
947 the model code, carried out the simulations, and computed the model performance statistics. DB, WS, MR, MT, and
948 RB analyzed the data. RB wrote the manuscript draft; DB, MR, and WS reviewed and edited the manuscript.

949 **Competing interests**

950 The authors declare that they have no conflict of interest.

951 **Disclaimer**

952 Any use of trade, firm, or product names is for descriptive purposes only and does not imply endorsement by the U.S.
953 Government.

954 **Acknowledgements**

955 Adrian Lewis compiled and summarized geotechnical data from published and publicly available sources. Mason
956 Einbund extracted statistics on landslide true positives and density from pre-Hurricane Maria factor of safety grids.
957 Emily Bedinger generated flow-accumulation raster grids and edited the model output grids to remove edge effects.
958 Brian Collins and Lauren Schaefer reviewed an earlier version of this manuscript. This work was supported in part by
959 the Additional Supplemental Appropriations for Disaster Relief Requirements Act, 2018 (P.L. 115-123)



960 **References**

- 961 Aaron, J., McDougall, S., Moore, J.R., Coe, J.A., and Hungr, O.: The role of initial coherence and path materials in
962 the dynamics of three rock avalanche case histories, *Geoenvironmental Disasters*, 4, 5. [https://doi.org/10.1186/s40677-](https://doi.org/10.1186/s40677-017-0070-4)
963 [017-0070-4](https://doi.org/10.1186/s40677-017-0070-4), 2017.
- 964 Alvioli, M., and Baum, R.L.: Parallelization of the TRIGRS model for rainfall-induced landslides using the message
965 passing interface. *Environ. Modell. Softw.* 81, 122–135. <https://doi.org/10.1016/j.envsoft.2016.04.002>, 2016.
- 966 ASTM International: D2487-17e1, Standard Practice for Classification of Soils for Engineering Purposes (Unified
967 Soil Classification System), <https://doi.org/10.1520/D2487-17E01>, 2020.
- 968 Baum, R.L.: Rapid sensitivity analysis for reducing uncertainty in landslide hazard assessments, in: *Understanding
969 and Reducing Landslide Disaster Risk*, edited by: Guzzetti, F., Mihalić Arbanas, S., Reichenbach, P., Sassa, K.,
970 Bobrowsky, P.T., and Takara, K., Springer, Cham, Switzerland, 329–335, [https://doi.org/10.1007/978-3-030-60227-](https://doi.org/10.1007/978-3-030-60227-7_37)
971 [7_37](https://doi.org/10.1007/978-3-030-60227-7_37), 2021.
- 972 Baum, R.L.: Slabs3D—A Fortran 95 program for analyzing potential shallow landslides in a digital landscape, U.S.
973 Geol. Surv. software release [code], <https://doi.org/10.5066/P9G4I8IU>, 2023.
- 974 Baum, R.L., and Lewis, A.C.: Engineering soil classification and geotechnical measurements in Lares, Naranjito, and
975 Utuado, Puerto Rico: U.S. Geol. Surv. data release [data set], <https://doi.org/10.5066/P9UXTQ4B>, 2023.
- 976 Baum, R.L., Brien, D.L., Reid, M.E., Schulz, W.H., Tello, M.J., and Bedinger, E.C.: Model input and output data
977 covering Lares Municipio, Utuado Municipio, and Naranjito Municipio, Puerto Rico, for landslide initiation
978 susceptibility assessment after Hurricane Maria: U.S. Geol. Surv. data release [data set],
979 <https://doi.org/10.5066/P9C1U0LP>, 2023.
- 980 Baum, R.L., Savage, W.Z., and Godt, J.W.: TRIGRS—A Fortran program for transient rainfall infiltration and grid-
981 based regional slope-stability analysis, version 2.0, U.S. Geol. Surv. Open-File Report 2008-1159, 75 pp.
982 <https://doi.org/10.3133/ofr20081159>, 2008.
- 983 Baum, R.L., Godt, J.W., and Savage, W.Z.: Estimating the timing and location of shallow rainfall-induced landslides
984 using a model for transient, unsaturated infiltration. *Journal of Geophysical Research: Earth Surface*, 115(F3), F03013.
985 <https://doi.org/10.1029/2009JF001321>, 2010.
- 986 Baum, R.L., Godt, J.W., Coe, J.A., and Reid, M.E.: Assessment of shallow landslide potential using 1D and 3D slope
987 stability analysis, in: *Landslides and Engineered Slopes: Protecting Society through Improved Understanding*, edited
988 by: Eberhardt, E., Froese, C., Turner, A.K., and Leroueil, S., Taylor & Francis Group, London, pp. 1667–1672, ISBN
989 978-0-415-62123-6, 2012.
- 990 Baum, R.L., Schulz, W.H., Brien, D.L., Burns, W.L., Reid, M.E., and Godt, J.W.: Progress in regional landslide hazard
991 assessment—Examples from the USA, in: *Landslide Science for a Safer Geoenvironment*, edited by, Sassa, K.,
992 Canuti, P., and Yin, Y., Springer, Cham, Switzerland, pp. 21–36. https://doi.org/10.1007/978-3-319-04999-1_2, 2014.
- 993 Baum, R.L., Cerovski-Darriau, C., Schulz, W.H., Bessette-Kirton, E., Coe, J.A., Smith, J.B., and Smoczyk, G.M.:
994 Variability of hurricane María debris-flow source areas in Puerto Rico—Implications for hazard assessment, AGU
995 Fall Meeting, Washington, DC 2018, NH14A-02, <https://agu.confex.com/agu/fm18/meetingapp.cgi/Paper/412740>,
996 2018.



- 997 Baum, R.L., Scheevel, C.R., and Jones, E.S.: Constraining parameter uncertainty in modeling debris-flow initiation
998 during the September 2013 Colorado Front Range storm, in: Debris-flow Hazards Mitigation: Mechanics, Monitoring,
999 Modeling, and Assessment, edited by: Kean, J.W., Coe, J.A., Santi, P.M., and Guillen, B.K., Association of
1000 Environmental and Engineering , Brunswick, Ohio, pp. 249–256, <https://doi.org/10.25676/11124/173212>, 2019.
- 1001 Baum, R.L., Bedinger, E.C., and Tello, M.J.: REGOLITH--A Fortran 95 program for estimating soil mantle thickness
1002 in a digital landscape for landslide and debris-flow hazard assessment, U.S. Geol. Surv. software release [code],
1003 <https://doi.org/10.5066/P9U2RDWJ>, 2021.
- 1004 Bawiec, W.J.: Geologic terranes of Puerto Rico, in: Geology, geochemistry, geophysics, mineral occurrences, and
1005 mineral resource assessment for the commonwealth of Puerto Rico, edited by: Bawiec W.J., U.S. Geol. Surv. Open-
1006 File Rep. 98–38. <https://doi.org/10.3133/ofr9838>, 1998.
- 1007 Baxstrom, K.W., Einbund, M.M., and Schulz, W.H.: Map data from landslides triggered by Hurricane María in a
1008 section of Naranjito, Puerto Rico, U.S. Geol. Surv. data release [data set], <https://doi.org/10.5066/P9GBGA4I>, 2021a.
- 1009 Baxstrom, K.W., Einbund, M.M., and Schulz, W.H.: Map data from landslides triggered by Hurricane María in the
1010 greater karst region of northwest Puerto Rico, U.S. Geol. Surv. data release [data set],
1011 <https://doi.org/10.5066/P9YYU7W1>, 2021b.
- 1012 Begueria, S.: Validation and evaluation of predictive models in hazard assessment and risk management. *Nat. Hazards*,
1013 37, 315–329. <https://doi.org/10.1007/s11069-005-5182-6>, 2006.
- 1014 Benda, L., Miller, D., Andras, K., Bigelow, P., Reeves, G., and Michael, D.: NetMap: A new tool in support of
1015 watershed science and resource management, *Forest Sci.*, 53(2), 206–219.
1016 <https://doi.org/10.1093/forestscience/53.2.206>, 2007.
- 1017 Bessette-Kirton, E.K., Coe, J.A., Godt, J.W., Kean, J.W., Rengers, F.K., Schulz, W.H., Baum, R.L., Jones, E.S., and
1018 Staley, D.M.: Map data showing concentration of landslides caused by hurricane María in Puerto Rico. U.S. Geol.
1019 Surv. data release [data set], <https://doi.org/10.5066/F7JD4VRF>, 2017.
- 1020 Bessette-Kirton, E.K., Cerovski-Darriau, C., Schulz, W.H., Coe, J.A., Kean, J.W., Godt, J.W., Thomas, M.A., and
1021 Hughes, K.S.: Landslides triggered by Hurricane María: Assessment of an extreme event in Puerto Rico, *GSA Today*,
1022 29, 4–10. <https://doi.org/10.1130/GSATG383A.1>, 2019a.
- 1023 Bessette-Kirton, E.K., Kean, J.W., Coe, J.A., Rengers, F.K., and Staley, D.M.: An evaluation of debris-flow runoff
1024 model accuracy and complexity in Montecito, California: Towards a framework for regional inundation-hazard
1025 forecasting, in: Debris-flow Hazards Mitigation: Mechanics, Monitoring, Modeling, and Assessment, edited by: Kean,
1026 J.W., Coe, J.A., Santi, P.M., Guillen, B.K., Association of Environmental and Engineering Geologists, Brunswick,
1027 Ohio, pp. 257–264. <https://doi.org/10.25676/11124/173211>, 2019b.
- 1028 Bessette-Kirton, E.K., Coe, J.A., Kelly, M.A., Cerovski-Darriau, C., and Schulz, W.H.: Map data from landslides
1029 triggered by Hurricane María in four study areas of Puerto Rico. U.S. Geol. Surv. data release [data set].
1030 <https://doi.org/10.5066/P9OW4SLX>, 2019c.
- 1031 Bessette-Kirton, E.K., Coe, J.A., Schulz, W.H., Cerovski-Darriau, C., and Einbund, M.M.: Mobility characteristics of
1032 debris slides and flows triggered by Hurricane María in Puerto Rico, *Landslides* 17, 2795–2809,
1033 <https://doi.org/10.1007/s10346-020-01445-z>, 2020.



- 1034 Brien, D.L., Reid, M.E., Cronkite-Ratcliff, C., and Perkins, J.P.: Portraying runout and inundation from hurricane-
1035 induced landslides in Puerto Rico, *Geological Society of America Abstracts with Programs*. 53(6), 85-4,
1036 <https://doi.org/10.1130/abs/2021AM-368632>, 2021.
- 1037 Catani, F., Segoni, S., and Falorni, G.: An empirical geomorphology-based approach to the spatial prediction of soil
1038 thickness at catchment scale, *Water Resour. Res.*, 46(5), W05508, <https://doi.org/10.1029/2008WR007450>, 2010.
- 1039 Canli, E., Mergili, M., Thiebes, B., and Glade, T.: Probabilistic landslide ensemble prediction systems: Lessons to be
1040 learned from hydrology, *Nat. Hazard. Earth Sys.*, 18(8), 2183–2202, <https://doi.org/10.5194/nhess-18-2183-2018>,
1041 2018.
- 1042 Carrara, A., Guzzetti, F., Cardinali, M., and Reichenbach, P.: Use of GIS technology in the prediction and monitoring
1043 of landslide hazard, *Nat. Hazards*, 20, 117–135, <https://doi.org/10.1023/A:1008097111310>, 1999.
- 1044 Chung, C.F., and Fabbri, A.G.: Validation of spatial prediction models for landslide hazard mapping, *Nat. Hazards*,
1045 30, 451–472, <https://doi.org/10.1023/B:NHAZ.0000007172.62651.2b>, 2003.
- 1046 Einbund, M.M., Baxstrom, K.S., and Schulz, W.H.: Map data from landslides triggered by Hurricane María in four
1047 study areas in the Utuado municipality, Puerto Rico, U.S. Geol. Surv. data release [data set],
1048 <https://doi.org/10.5066/P9ZNUR1P>, 2021a.
- 1049 Einbund, M.M., Baxstrom, K.S., and Schulz, W.H.: Map data from landslides triggered by Hurricane María in four
1050 study areas in the Lares municipality, Puerto Rico. U.S. Geol. Surv. data release [data set],
1051 <https://doi.org/10.5066/P9EASZZ7>, 2021b.
- 1052 Ellen, S.D., Mark, R.K., Cannon, S.H., and Knifong, D.L.: Map of debris-flow hazard in the Honolulu District of
1053 Oahu, Hawaii, U.S. Geol. Surv. Open-File Rep. 93-213, 28 pp., <https://doi.org/10.3133/ofr93213>, 1993.
- 1054 Fan, L., Lehmann, P., McArdell, B., and Or, D.: Linking rainfall-induced landslides with debris flows runout patterns
1055 towards catchment scale hazard assessment, *Geomorphology* 280, 1-15.
1056 <https://doi.org/10.1016/j.geomorph.2016.10.007>, 2017.
- 1057 Fawcett, T.: An introduction to ROC analysis, *Pattern Recogn. Lett.*, 27(8), 861–874,
1058 <https://doi.org/10.1016/j.patrec.2005.10.010>, 2006.
- 1059 George, D.L., and Iverson, R.M.: A depth-averaged debris-flow model that includes the effects of evolving dilatancy:
1060 2. Numerical predictions and experimental tests, *P. Roy. Soc. A-Math. Phys.*, 470(2170), 20130820,
1061 <https://doi.org/10.1098/rspa.2013.0820>, 2014.
- 1062 Godt, J.W., Schulz, W.H., Baum, R.L., and Savage, W.Z.: Modeling rainfall conditions for shallow landsliding in
1063 Seattle, Washington, in: *Landslides and Engineering Geology of the Seattle, Washington, Area*, edited by: Baum,
1064 R.L., Godt, J.W., Highland, L.M., Geological Society of America, Boulder, Colorado, 137–152,
1065 [https://doi.org/10.1130/2008.4020\(08\)](https://doi.org/10.1130/2008.4020(08)), 2008.
- 1066 Gomes, G.J.C., Vrugt, J.A., and Vargas, Jr., E.A.: Toward improved prediction of the bedrock depth underneath
1067 hillslopes: Bayesian inference of the bottom-up control hypothesis using high-resolution topographic data, *Water*
1068 *Resour. Res.*, 52(4), 3085–3112, <https://doi.org/10.1002/2015WR018147>, 2016.



- 1069 Gupta, H.V., Kling, H., Yilmaz, K.K., and Martinez, G.F.: Decomposition of the mean squared error and NSE
1070 performance criteria: Implications for improving hydrological modeling. *J. Hydrol.*, 377(1-2), 80–91.
1071 <https://doi.org/10.1016/j.jhydrol.2009.08.003>, 2009.
- 1072 Ho, J.-Y., Lee, K.T., Chang, T.-C., Wang, Z.-Y., and Liao, Y.-H.: Influences of spatial distribution of soil thickness
1073 on shallow landslide prediction. *Eng. Geol.*, 124, 38–46. <https://doi.org/10.1016/j.enggeo.2011.09.013>, 2012.
- 1074 Hovland, H.J.: Three-dimensional slope stability analysis method. *J. Geotech. Eng.-ASCE*, 103(GT9), 971–986.
1075 <https://doi.org/10.1061/AJGEB6.0000493>, 1977.
- 1076 Hsu, Y.C., and Liu, K.F.: Combining TRIGRS and DEBRIS-2D models for the simulation of a rainfall infiltration
1077 induced shallow landslide and subsequent debris flow, *Water*, 11(5), 890, <https://doi.org/10.3390/w11050890>, 2019.
- 1078 Hughes, K.S., Bayouth-García, D., Martínez-Milian, G.O., Schulz, W.H., and Baum, R.L.: Map of slope-failure
1079 locations in Puerto Rico after Hurricane María. U.S. Geol. Surv. data release [data set],
1080 <https://doi.org/10.5066/P9BVM74>, 2019.
- 1081 Hughes, K.S., and Schulz, W.H.: Map depicting susceptibility to landslides triggered by intense rainfall, Puerto Rico,
1082 U.S. Geol. Surv. Open-File Rep. 2020–1022, 91 pp., 1 plate, scale 1:150,000. <https://doi.org/10.3133/ofr20201022>,
1083 2020a.
- 1084 Hughes, K.S., Schulz, W.H.: Results from frequency-ratio analyses of soil classification and land use related to
1085 landslide locations in Puerto Rico following Hurricane María. U.S. Geol. Surv. data release [data set],
1086 <https://doi.org/10.5066/P9VK2FAL>, 2020b.
- 1087 Hungr, O., Salgado, F.M., and Byrne, P.M.: Evaluation of a three-dimensional method of slope-stability analysis, *Can.*
1088 *Geotech. J.*, 26(4), 679–686, <https://doi.org/10.1139/t89-079>, 1989.
- 1089 Iverson, R.M.: Landslide triggering by rain infiltration, *Water Resour. Res.*, 36(7), 1897–1910,
1090 <https://doi.org/10.1029/2000WR900090>, 2000.
- 1091 Jibson, R.W.: Debris flows in southern Puerto Rico, in: *Landslide processes of the eastern United States and Puerto*
1092 *Rico*, edited by: Schultz A.P., and Jibson R.W., *Geol. S. Am. S.*, 236, 29–55, <https://doi.org/10.1130/SPE236-p29>,
1093 1989.
- 1094 Jolly, W.T., Lidiak, E.G., Dickin, A.P., and Wu, T.-W.: Geochemical diversity of Mesozoic island arc tectonic blocks
1095 in eastern Puerto Rico, in: *Tectonics and Geochemistry of the Northeastern Caribbean*, edited by: Likiak, E.G., Larue,
1096 D.K., *Geol. S. Am. S.*, 322, 67–98, <https://doi.org/10.1130/0-8137-2322-1.67>, 1998.
- 1097 Lambe, T.W., and Whitman, R.V.: *Soil Mechanics*, John Wiley & Sons, New York, 553 pp., ISBN 0471511927, 1969.
- 1098 Larsen, M.C., and Torres-Sanchez, A.J.: Landslides triggered by hurricane Hugo in eastern Puerto Rico, September
1099 1989. *Caribb. J. Sci.*, 28(3-4), 113–125, 1992.
- 1100 Larsen, M.C., and Simon, A.: A rainfall intensity-duration threshold for landslides in a humid-tropical environment,
1101 Puerto Rico, *Geogr. Ann. A*, 75(1-2), 13-23, <https://doi.org/10.1080/04353676.1993.11880379>, 1993.
- 1102 Larsen, M.C., and Parks, J.E.: Map showing landslide susceptibility in the Comerio municipality, Puerto Rico, U.S.
1103 Geol. Surv. Open-File Rep. 98-566, 1 plate, scale 1:20,000. <https://doi.org/10.3133/ofr98566>, 1998.
- 1104 Larsen, M.C., and Torres-Sanchez, A.J.: The frequency and distribution of recent landslides in three montane tropical
1105 regions of Puerto Rico, *Geomorphology*, 24(4), 309–331, [https://doi.org/10.1016/S0169-555X\(98\)00023-3](https://doi.org/10.1016/S0169-555X(98)00023-3), 1998.



- 1106 Larsen M.C., Santiago, M., Jibson, R., and Questell, E.: Map showing susceptibility to rainfall-triggered landslides in
1107 the municipality of Ponce, Puerto Rico, U.S. Geol. Surv. Scientific Investigations Map 2818, 1 plate, scale 1:30,000,
1108 <https://doi.org/10.3133/sim2818>, 2004.
- 1109 Larsen, M.C.: Landslides and sediment budgets in four watersheds in eastern Puerto Rico, in: Water Quality and
1110 Landscape Processes of Four Watersheds in Eastern Puerto Rico, edited by: Murphy, S.F., and Stallard, R.F., U.S.
1111 Geol. Surv. Prof. Paper 1789, 153–178, <https://doi.org/10.3133/pp1789>, 2012.
- 1112 Lee, S., Ryu, J.-H., Min, K., and Won, J.-S.: Landslide susceptibility analysis using GIS and artificial neural network,
1113 *Earth Surf. Proc. Land.*, 28(12), 1361–1376, <https://doi.org/10.1002/esp.593>, 2003.
- 1114 Lepore, C., Kamal, S.A., Shanahan, P., and Bras, R.L.: Rainfall-induced landslide susceptibility zonation of Puerto
1115 Rico, *Environ. Earth Sci.*, 66, 1667–1681, <https://doi.org/10.1007/s12665-011-0976-1>, 2012.
- 1116 Lepore, C., Arnone, E., Noto, L.V., Sivandran, G., and Bras, R.L.: Physically based modeling of rainfall-triggered
1117 landslides: A case study in the Luquillo forest, Puerto Rico, *Hydrol. Earth Syst. Sci.*, 17(9), 3371–3387,
1118 <https://doi.org/10.5194/hess-17-3371-2013>, 2013.
- 1119 Likos, W.J., Wayllace, A., Godt, J., and Lu, N.: Modified direct shear apparatus for unsaturated sands at low suction
1120 and stress, *Geotech. Test. J.*, 33(4), 286–298, <https://doi.org/10.1520/GTJ102927>, 2010.
- 1121 Mergili, M., Schwarz, L., and Kociu, A.: Combining release and runoff in statistical landslide susceptibility modeling,
1122 *Landslides*, 16(11), 2151–2165, <https://doi.org/10.1007/s10346-019-01222-7>, 2019.
- 1123 Murphy, S.F., Stallard, R.F., Larsen, M.C., and Gould, W.A.: Physiography, geology, and land cover of four
1124 watersheds in eastern Puerto Rico, U.S. Geol. Surv. Prof. Paper 1789-A, 24 pp., <https://doi.org/10.3133/pp1789A>,
1125 2012.
- 1126 Monroe, W.H.: The karst landforms of Puerto Rico, U.S. Geol. Surv. Prof. Paper 899, 69 pp.,
1127 <https://doi.org/10.3133/pp899>, 1976.
- 1128 Nicótina, L., Tarboton, D.G., Tesfa, T.K., and Rinaldo, A.: Hydrologic controls on equilibrium soil depths, *Water*
1129 *Resour. Res.*, 47(4), W04517, <https://doi.org/10.1029/2010WR009538>, 2011.
- 1130 Pando, M.A., Ruiz, M.E., and Larsen, M.C.: Rainfall-induced landslides in Puerto Rico: An overview, in: Slopes and
1131 Retaining Structures Under Seismic and Static Conditions, edited by Gabr, M.A., Bowders, J.J., Elton, D., and
1132 Zornberg, J.G., ASCE Geotech. SP., 140, 2911–2925, [https://doi.org/10.1061/40787\(166\)25](https://doi.org/10.1061/40787(166)25), 2005.
- 1133 Patton, N.R., Lohse, K.A., Godsey, S.E., Crosby, B.T., and Seyfried, M.S.: Predicting soil thickness on soil mantled
1134 hillslopes, *Nat. Commun.*, 9, 3329, <https://doi.org/10.1038/s41467-018-05743-y>, 2018.
- 1135 Pelletier, J.D., and Rasmussen, C.: Geomorphically based predictive mapping of soil thickness in upland watersheds,
1136 *Water Resour. Res.*, 45(9):W09417. <https://doi.org/10.1029/2008WR007319>, 2009.
- 1137 Perkins, J.P., Baxstrom, K.W., Einbund, M.M, and Schulz, W.H: Modified basal contact of the Tertiary Lares
1138 Limestone in the vicinity of Utuado, Puerto Rico, USA, derived from USGS Open-File Report 98-038, U.S. Geol.
1139 Surv. data release [data set], <https://doi.org/10.5066/P9NL9EZG>, 2022.
- 1140 Raia, S., Alvioli, M., Rossi, M., Baum, R.L., Godt, J.W., and Guzzetti F.: Improving predictive power of physically
1141 based rainfall-induced shallow landslide models: A probabilistic approach, *Geosci. Model Dev.*, 7(2), 495–514,
1142 <https://doi.org/10.5194/gmd-7-495-2014>, 2014.



- 1143 Ramos-Scharrón, C.E., Arima, E.Y., Guidry, A., Ruffe, D., and Vest B.: Sediment mobilization by hurricane-driven
1144 shallow landsliding in a wet subtropical watershed, *J. Geophys. Res.-Earth*, 126(5), e2020JF006054,
1145 <https://doi.org/10.1029/2020JF006054>, 2021.
- 1146 Reid, M.E., Christian, S.B., Brien, D.L., and Henderson, S.T.: Scoops3D—Software to analyze 3D slope stability
1147 throughout a digital landscape, *U.S. Geol. Surv. Techniques and Methods 14-A1 [code]*, 218 pp.
1148 <https://doi.org/10.3133/tm14A1>, 2015.
- 1149 Reid, M.E., Coe, J.A., and Brien, D.L.: Forecasting inundation from debris flows that grow volumetrically during
1150 travel, with application to the Oregon coast range, USA, *Geomorphology*, 273, 396–411.
1151 <https://doi.org/10.1016/j.geomorph.2016.07.039>, 2016.
- 1152 Roering, J.J.: How well can hillslope evolution models “explain” topography? *Geol. Soc. Am. Bull.*, 120(9-10), 1248–
1153 1262, <https://doi.org/10.1130/B26283.1>, 2008.
- 1154 Schulz, W.H., Jensen, E.K., Cerovski-Darriau, C.R., Baum, R.L., Thomas, M.A., and Coe, J.A.: Field observations of
1155 landslides and related materials following Hurricane Maria, Puerto Rico, U.S. Geol. Surv. data release [data set],
1156 <https://doi.org/10.5066/P9T9KZ6T>, 2023.
- 1157 Simon, A., Larsen, M.C., and Hupp, C.R.: The role of soil processes in determining mechanisms of slope failure and
1158 hillslope development in a humid-tropical forest eastern Puerto Rico, *Geomorphology*, 3(3-4), 263–286,
1159 [https://doi.org/10.1016/0169-555X\(90\)90007-D](https://doi.org/10.1016/0169-555X(90)90007-D), 1990.
- 1160 Smith, J.B., Thomas, M.A., Ashland, F., Michel, A.R., Wayllace, A., and Mirus, B.B.: Hillslope hydrologic
1161 monitoring data following Hurricane María in 2017, Puerto Rico, July 2018 to June 2020, U.S. Geol. Surv. data release
1162 [data set], <https://doi.org/10.5066/P9548YK2>, 2020.
- 1163 Soil Survey Staff: Soil Survey Geographic (SSURGO) Database for Puerto Rico, all regions. U.S. Department of
1164 Agriculture Natural Resources Conservation Service [data set], <https://websoilsurvey.sc.egov.usda.gov/app/> (last
1165 access: 10 August 2023), 2018.
- 1166 Sowers, G.F.: Landslides in weathered volcanics in Puerto Rico, in: *Proceedings of the Fourth Pan-American*
1167 *Conference on Soil Mechanics and Foundation Engineering*, American Society of Civil Engineers, New York, 105–
1168 115, 1971.
- 1169 Taggart, B.E., and Joyce, J.: Radiometrically dated marine terraces on northwestern Puerto Rico, in: *Transactions of*
1170 *the 12th Caribbean Geological Conference*, St. Croix, U.S. Virgin Islands, August 7th-11th, 1989, Miami Geological
1171 Society, South Miami, Florida, 248–258, 1991.
- 1172 Taylor, D.W.: *Fundamentals of Soil Mechanics*, John Wiley & Sons, New York, 700 pp., 1948.
- 1173 Thomas, M.A., and Cerovski-Darriau, C.: Infiltration data collected post-Hurricane María across landslide source area
1174 materials, Puerto Rico, USA, U.S. Geol. Surv. data release [data set], <https://doi.org/10.5066/P9SCGVF7>, 2019.
- 1175 Tello, M.: Optimization of landslide susceptibility modeling: A Puerto Rico case study, Master of Science Thesis,
1176 Colorado School of Mines, Golden, Colorado, <https://hdl.handle.net/11124/174137>, 2020.
- 1177 Terzaghi, K., Peck, R.B., and Mesri, G.: *Soil Mechanics in Engineering Practice*, 3rd ed. John Wiley & Sons: New
1178 York, 549 pp., ISBN: 978-0-471-08658-1, 1996.



- 1179 Turnbull, W.J., and Hvorslev, M.J.: Special problems in slope stability, *Journal of the Soil Mechanics and Foundations*
1180 *Division*, 93(SM4), 499–528, <https://doi.org/10.1061/JSFEAQ.0001004>, 1967.
- 1181 U.S. Geological Survey: 2015–2016 USGS Puerto Rico LiDAR (project PR_PuertoRico_2015) [data set], at
1182 <https://apps.nationalmap.gov/lidar-explorer/#/> (last access: 10 August 2023), 2018.
- 1183 U.S. Geological Survey: 2018 USGS Puerto Rico – Virgin Islands LiDAR (project PR_PRVI_A_2018),
1184 <https://apps.nationalmap.gov/lidar-explorer/#/> (last access: 10 August 2023), 2020a.
- 1185 U.S. Geological Survey: 2018 USGS Puerto Rico – Virgin Islands LiDAR (project PR_PRVI_D_2018),
1186 <https://apps.nationalmap.gov/lidar-explorer/#/> (last access: 10 August 2023), 2020b.
- 1187 U.S. Geological Survey: 2018 USGS Puerto Rico – Virgin Islands LiDAR (project PR_PRVI_H_2018),
1188 <https://apps.nationalmap.gov/lidar-explorer/#/> (last access: 10 August 2023), 2020c.
- 1189 Zieher, T., Rutzinger, M., Schneider-Muntau, B., Perzl, F., Leidinger, D., Formayer, H., and Geitner, C.: Sensitivity
1190 analysis and calibration of a dynamic physically based slope stability model, *Nat. Hazard. Earth Sys.*, 17(6), 971–992.
1191 <https://doi.org/10.5194/nhess-17-971-2017>, 2017.
- 1192